Dissecting human monoclonal antibody responses from mRNA- and protein-based XBB.1.5 COVID-19 monovalent vaccines

Raianna F. Fantin[1,2*], Jordan J. Clark[1,2*], Hallie Cohn[1,2*], Deepika Jaiswal[1*], Bailey Bozarth[1,2*], Alesandro Civljak[1], Vishal Rao[1,2,3], Igor Lobo[1,2], Jessica R. Nardulli[1,2], Komal Srivastava[1,2], Jeremy Yong[1,2], Robert Andreata-Santos[1,2,4], Kaitlyn Bushfield[1,2], Edward S. Lee[5,6], Gagandeep Singh[1,2], PVI Study Group[1,2,7], Steven H. Kleinstein[5,8], Florian Krammer[1,2,7,9†], Viviana Simon[1,2,7,10,11†], Goran Bajic[1†], Camila H. Coelho [1,2,12†]

1. Department of Microbiology, Icahn School of Medicine at Mount Sinai, New York, NY, USA
2. Center for Vaccine Research and Pandemic Preparedness, Icahn School of Medicine at Mount Sinai, New York, NY, USA
3. Graduate School of Biomedical Sciences, Icahn School of Medicine at Mount Sinai, New York, NY, 10029, USA
4. Retrovirology Laboratory, Department of Microbiology, Immunology and Parasitology, Paulista School of Medicine, Federal University of São Paulo (UNIFESP), São Paulo, Brazil
5. Department of Laboratory Medicine, Yale School of Medicine, New Haven, CT, 06520, USA
6. Department of Pathology, Yale School of Medicine, New Haven, CT 06520, USA
7. Department of Pathology, Molecular and Cell-Based Medicine, Icahn School of Medicine at Mount Sinai, New York, NY, USA
8. Program in Computational Biology and Biomedical Informatics, Yale University, New Haven, CT 06520, USA
9. Ignaz Semmelweis Institute, Interuniversity Institute for Infection Research, Medical University of Vienna, Vienna, Austria
10. The Global Health and Emerging Pathogens Institute, Icahn School of Medicine at Mount Sinai, New York, NY, USA
11. Division of Infectious Diseases, Department of Medicine, Icahn School of Medicine at Mount Sinai, New York, NY, USA
12. Precision Immunology Institute, Icahn School of Medicine at Mount Sinai, New York, NY, USA

*These authors contributed equally

†Corresponding authors: camila.coelho@mssm.edu, goran.bajic@mssm.edu, viviana.simon@mssm.edu, florian.krammer@mssm.edu

Address: 1 Gustave Levy Place, Annenberg, 16th floor - New York, NY 10029

40 GRAPHICAL ABSTRACT

41
42
43
44
45
46
47
48
49
50
51
52
53
54
55
56
57
58
59
60
61
62
63
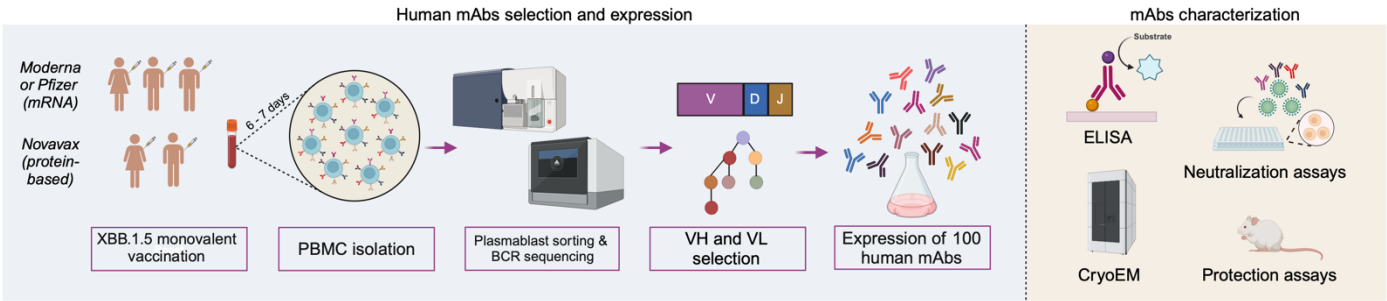
64 ABSTRACT

65 The emergence of highly contagious and immune-evasive severe acute respiratory

66 syndrome coronavirus 2 (SARS-CoV-2) variants has required reformulation of coronavirus

67 disease 2019 (COVID-19) vaccines to target those new variants specifically. While previous

68 infections and booster vaccinations can enhance variant neutralization, it is unclear whether

69 the monovalent version, administered using either mRNA or protein-based vaccine

70 platforms, can elicit *de novo* B-cell responses specific for Omicron XBB.1.5 variants. Here,

71 we dissected the genetic antibody repertoire of 603 individual plasmablasts derived from

72 five individuals who received a monovalent XBB.1.5 vaccination either with mRNA (Moderna

73 or Pfizer/BioNtech) or adjuvanted protein (Novavax). From these sequences, we expressed

74 100 human monoclonal antibodies and determined binding, affinity and protective potential

75 against several SARS-CoV-2 variants, including JN.1. We then select two vaccine-induced

76 XBB.1.5 mAbs, M2 and M39. M2 mAb was a *de novo,* antibody, i.e., specific for XBB.1.5 but

77 not ancestral SARS-CoV-2. M39 bound and neutralized both XBB.1.5 and JN.1 strains. Our

78 high-resolution cryo-electron microscopy (EM) structures of M2 and M39 in complex with the

79 XBB.1.5 spike glycoprotein defined the epitopes engaged and revealed the molecular

80 determinants for the mAbs' specificity. These data show, at the molecular level, that

81 monovalent, variant-specific vaccines can elicit functional antibodies, and shed light on

82 potential functional and genetic differences of mAbs induced by vaccinations with different

83 vaccine platforms.

84

85

86 KEYWORDS: mRNA vaccines; Novavax; monovalent XBB.1.5; SARS-CoV-2 mAbs; cryo-EM

87

88

89

90

INTRODUCTION

The spike (S) protein of SARS-CoV-2 has proven to be an essential target for human-neutralizing antibodies(1–8). However, spike continues to accumulate mutations, creating new viral variants of concern (VOCs) that often exhibit increased transmissibility and a greater ability to evade the host immune system(9–11). Specifically, the Omicron variant of SARS-CoV-2 accrued multiple amino acid mutations within spike and became particularly resistant to neutralization following primary vaccination(9, 12–14). Omicron's evasion of previously elicited antibodies and its development into further antibody-resistant subvariants led to the development of bivalent vaccines(15). Among the most recent subvariants, XBB.1.5 became widely recognized for containing key mutations that allow evasion of host immune responses induced by booster vaccinations(16, 17). To target the circulating XBB.1.5 strain, the US Food and Drug Administration (FDA) approved updated mRNA monovalent vaccines (*Pfizer or Moderna*) along with a protein-based version adjuvanted with Matrix M™ (*Novavax*) in the fall of 2023(18, 19). It is not yet clear whether the functional monoclonal antibodies elicited in response to monovalent Omicron-specific vaccines targeting XBB.1.5 SARS-CoV-2 represent *de novo* responses or reflect cross-reactivity acquired from previous exposures. Therefore, it became critical to evaluate the ability of monovalent SARS-CoV-2 Omicron-specific vaccines to produce antibodies that recognize those viral variant epitopes. Here, we assessed the human antibody repertoire of plasmablasts from adult participants receiving the mRNA-based (Pfizer, Moderna; 3 participants) or protein-based (Novavax; 2 participants) XBB.1.5 SARS-CoV-2 vaccine. This work reveals novel epitopes of *de novo* and cross-reactive (ancestral and XBB.1.5) antibodies elicited by monovalent XBB.1.5-specific SARS-CoV-2 immunizations.

117 RESULTS

118 *IGHA and IGHG are the predominant isotypes elicited by XBB.1.5 SARS-CoV-2 monovalent*
119 *vaccines*

120 The antibody repertoire was obtained from five different participants (sex ratio of 1.5:1;

121 male:female). They all had 5-6 prior SARS-CoV-2 vaccinations (primary ancestral scheme

122 consisting of two doses, ancestral SARS-CoV-2, and bivalent booster vaccinations, and the

123 XBB.1.5 monovalent vaccine) (Fig. 1). After pairing and filtering 213 mRNA vaccine-induced

124 and 390 protein vaccine-induced paired heavy and light chain sequences of single cell

125 plasmablasts (Table S1), we compared somatic hypermutation (SHM) levels in the heavy and

126 light chain V genes between the protein and mRNA groups. For both the heavy and light

127 chains (kappa and lambda), the highest SHM rates were found in the protein-based group

128 (Fig. S1a; $p \leq 0.0001$). VH mutations in the recombinant protein vaccine group had a median

129 frequency of 8.3%. The mRNA vaccine group presented a lower median mutation frequency

130 of 5.9%, with the top 25% of cells ranging from 8.1% to 15.6%. VL kappa and lambda median

131 mutation frequencies in the recombinant protein vaccine group were also the highest (5%

132 and 5.2%, respectively), with the top 25% of cells ranging between 7.5-25.3% and 7-15.1%

133 respectively. The mRNA vaccine cells showed even lower median mutation frequencies for

134 light chain: 2.6% and 3.8% for VL kappa and lambda, respectively, with the top 25% of cells

135 varying between 4.5-28% and 5.2-10%.

136 IGHA and IGHG are predominant isotypes in the repertoires of both groups, ranging from

137 42% to 58.5%; and 26.4% to 54.5% in the mRNA group, respectively. Similarly, in the

138 recombinant protein vaccine-induced plasmablasts, IGHA constitutes 50% - 57.9%, while

139 IGHG constitutes 34.3% - 45.5% of the BCR repertoires (Fig. S1b). The highest proportion

140 of IGHM was seen in the mRNA vaccine-induced plasmablasts, ranging from 3.41% to 15.1%.

141 For the protein group, IGHM ranged from 4% to 6.7%.

142 The highest median mutation frequencies in both groups were found in IGHA cells: 6.9% in

143 the mRNA vaccine-induced plasmablasts and 8.7% in the recombinant protein vaccine-

144　induced plasmablasts (Fig. S1c). At the IGHG1 isotype level, the recombinant protein

145　vaccine-induced plasmablasts also showed the highest SHM frequency values, with

146　significant differences between the groups (Fig. S1d; p ≤ 0.001, Mann-Whitney U test).

147　Clonal groups were determined by clustering BCR sequences that belonged to the same V

148　and J genes and had the same junction lengths, with a Hamming distance threshold of 0.15

149　applied for the nucleotide sequence of the heavy chain CDR3 regions. In the mRNA vaccine-

150　induced plasmablasts, we identified 164 clonal groups, encompassing 76.9% of the total

151　repertoire sequences, while the recombinant protein vaccine-induced plasmablasts had 289

152　clonal groups, representing 74.1% of the total repertoire sequences. Expanded clones

153　accounted for 5.2% of BCR sequences in the mRNA vaccine-induced plasmablasts and 6.6%

154　in the recombinant protein vaccine-induced plasmablasts.

155　Due to the high variability and critical antigen-binding function of the B cell heavy chain

156　CDR3 region, we examined both vaccine groups for physicochemical properties at the amino

157　acid level of the CDR3 region. The recombinant protein vaccine-induced plasmablasts

158　showed a slightly longer mean CDR3 region length than the mRNA vaccine-induced

159　plasmablasts (Fig. S1e; p ≤ 0.05, Mann-Whitney U test). Additionally, physicochemical

160　properties such as the aliphatic index (Fig. S1f; p ≤ 0.05, Mann-Whitney U test) were

161　significantly altered, with a slightly higher mean in the recombinant protein vaccine induced

162　plasmablasts. Conversely, the mRNA vaccine-induced plasmablasts exhibited heavy chain

163　CDR3 regions substantially more enriched in aromatic amino acids (Fig.S1g; p ≤ 0.01, Mann-

164　Whitney U test).

165

166 In summary, these results indicate that plasmablasts from both vaccine groups have similar

167 isotype compositions, with IGHA and IGHG being predominant.

168

169 *Assessment of the binding capacity of purified mAbs revealed multiple cross-reactive and*

170 *one XBB.1.5-specific antibody*

171 Participants were divided into groups based on the XBB.1.5 vaccine type: mRNA (Pfizer or

172 Moderna) or recombinant protein (Novavax), and paired VH-VL sequences were selected if

173 they either: (i) belonged to clonally expanded groups; or (ii) exhibited low levels of somatic

174 hypermutation, enhancing the likelihood of identifying *de novo* antibodies specific for

175 XBB.1.5. Based on these criteria, we synthesized and expressed 100 mAbs (50 from the

176 mRNA vaccine group and 50 from the recombinant protein vaccine group) that were then

177 screened for binding (Fig. S2).

178

179 To assess the binding capacity of the mAbs, we tested them in ELISA against ancestral,

180 XBB.1.5, and JN.1 SARS-CoV-2 spike as well as against ancestral, XBB.1.5 and JN.1 RBD. In

181 addition, we assessed binding to ancestral S1, S2, and NTD and an influenza virus H3

182 hemagglutinin which served as a negative control.

183 Eighteen binding mAbs were identified in the mRNA vaccine group: 16 bound to ancestral

184 spike (88.8%), 18 to XBB.1.5 spike (100%), 16 to JN.1 spike (88.8%), five to ancestral RBD

185 (27.8.%), four to XBB.1.5 RBD (22.2%) and three to JN.1 RBD (16.7%) (Fig. 2a – f). One of

186 the mRNA mAbs (M2) bound exclusively to XBB.1.5 Spike (5.5%) indicating that this mAb

187 was likely elicited through the most recent SARS-CoV-2 vaccination (Fig. 2b).

188 Three mAbs from the protein group bound to at least one SARS-CoV-2 antigen. Two of these

189 mAbs bound to ancestral spike (66.6%), and all three of them to XBB.1.5 and JN.1 spike

190 (100%) (Fig. 2a – c). There was no binding to the RBDs from any of the SARS-CoV-2 variants

191 tested (Fig. 2d - f).

192   When assessing subunits, 11 (61.1%), 12 (66.6%), and 9 (50%) mRNA vaccine group mAbs

193   bound to ancestral S1, S2, and NTD respectively. Within the recombinant protein vaccinated

194   group, one (33.3%) is bound to S1, and three of them (60%) bound to S2 and NTD (Fig. S3).

195   We selected 21 XBB.1.5 spike mAbs (mRNA; n=18 and protein-based; n=3) for neutralization

196   assays using authentic replication competent SARS-CoV-2 isolates (ancestral, XBB.1.5 and

197   JN.1). Four mAbs efficiently neutralized ancestral SARS-CoV-2, and one out of these four

198   (M27) also neutralized JN.1, but not XBB.1.5. M39 robustly neutralized XBB.1.5 and JN.1,

199   but not ancestral SARS-CoV-2 while M2 did not neutralize any variants *in vitro* (Fig. 2g – i).

200   Those three mAbs were then selected for *in vivo* protection assays. M2 as it was the only

201   XBB.1.5-specific mAb (*de novo*); M27 for its broad binding activity and its ability to neutralize

202   both the ancestral strain and JN.1 *in vitro* and M39 for neutralizing both XBB.1.5 and JN.1.

203

204   *M2, M27 and M39 fully protect against XBB.1.5 lethal SARS-CoV-2 challenge in a murine*
205   *model*

206   We investigated M2, M27, and M39's ability to protect *in vivo* using the hACE2-k18 lethal

207   SARS-CoV-2 murine challenge model *(20)*. Protection was assessed in a prophylactic setting

208   against ancestral SARS-CoV-2, XBB.1.5, and JN.1 variants via the passive transfer of

209   100mg/kg of mAb intraperitoneally, prior to intranasal infection with a lethal dose of

210   ancestral, XBB.1.5 or JN.1 SARS-CoV-2. M2 (the only XBB.1.5 specific mAb) was protective

211   against XBB.1.5 (100% survival, Figures 3b and 3e), but not against ancestral SARS-CoV-2

212   (Figures 3a and 3d) or JN.1 (Figures 3c and 3f). M27 (broadly binder) was capable of robust

213   protection from mortality against all viruses (100% of survival for ancestral and XBB.1.5 and

214   80% for JN.1) (Figures 3a – 3f), despite exhibiting a lack of XBB.1.5 neutralization *in vitro*.

215   For M39 (neutralizing XBB.1.5 and JN.1), full protection was observed when challenged with

216   XBB.1.5, with only partial protection for JN.1 (~60% of survival) (Figures 3b – 3f) and no

217   protection from ancestral SARS-CoV-2 (Figures 3a and 3d). Notably, M2 and M27 did not

218   neutralize XBB.1.5 *in vitro* but protected mice following challenge with XBB.1.5 SARS-CoV-

219   2. These data demonstrate that XBB.1.5 vaccine-elicited human mAbs can protect against

220   SARS-CoV-2 challenge in a murine model.

221

222   *Cryo-EM structure of M2 Fab and M39 Fab with SARS-CoV-2 XBB.1.5 spike*

223   To characterize the epitope of mAbs M2 and M39, and the intermolecular interactions at the

224   antibody-antigen interface, we used single-particle cryo-EM to determine the structure of

225   M2 Fab and M39 Fab in complex with SARS-CoV-2 XBB.1.5 spike. The structures show that

226   M2 Fab binds to the NTD while M39 binds to the RBD region of spike (Fig. 4a).

227   The global structure of the M2:spike complex shows three Fabs binding to one spike trimer

228   (Fig. S4), parallel to its 3-fold axis, and therefore suggests that M2 neutralizes the virus via

229   steric hindrance of the angiotensin-converting enzyme 2 (ACE2) receptor binding. M2 mAb

230   harbors a significant number of somatic hypermutations, with 14 and 12 amino acid

231   mutations in the heavy and light chain V-regions relative to their germline sequences,

232   respectively. Our focus refined map at 2.37 Å nominal resolution permitted us to build an

233   atomic model (Fig. 4b) and revealed that M2 engages NTD with both its heavy and light

234   chains. We note a cluster of tyrosine residues, Y33, Y52, Y53, and Y58, encoded by CDRH1

235   for the first and CDRH2 for the latter three. The four tyrosines engage in extensive polar and

236   non-polar interactions, primarily with the very N-terminus of spike (residues 14-17), including

237   the terminal pyroglutamate (Fig. 4d-e). Other notable heavy chain contacts, which arose

238   through somatic hypermutation, include S28N and S30N in the CDR1 (Fig. 4d-e, S6a). The

239   antibody light chain contacts NTD with residues derived both through somatic

240   hypermutation and from the germline, including Y48N and D50 (Fig. 4d, 4e). An important

241   interacting region on NTD appears to be the 140s loop bound by the M2 light chain CDRL1,

242   including main chain carbonyls from residues 29 and 30 and germline encoded Y31 side

243   chain, as well as CDRL2 including E49 derived through SHM.

244   The global structure of M39 indicated that it engages the RBD in the "up" as well as "down"

245   configuration. The global cryo-EM map showed three M39 Fabs bound with one spike trimer

246   - with 2 RBDs in the down, and 1 in the up configuration. We used the M39-bound down

247   RBD for further processing (Fig. S5e) and conducted local refinement of the M39 Fab/RBD

248   complex to identify the amino acid side-chain contacts at the antibody/antigen interface.

249   The locally refined map, at 2.65 Å nominal resolution, indicated that the M39 has a small

250   footprint on RBD involving CDRH1 and CDRH2 (Fig. 4c). All the polar contacts within the

251   antibody-antigen interface involve the Fab heavy chain, which forms hydrogen bonds with

252   RBD residues N439, K440, and Q506 (Fig.4f, 4g). These residues are conserved between all

253   variants of SARS-CoV-2 except the ancestral WA.1 which has an asparagine substitution at

254   position 440 (Fig. S6b). The primary amine of the K440 side-chain acts as a hydrogen bond

255   donor for D55 and D57 on M39 heavy chain and is thus the major interacting residue, which

256   explains the reduced binding of this antibody with the WA.1 variant. The relatively small

257   binding interface that is accessible on both the up and down RBD conformations likely

258   contributes to the cross-reactivity and potent neutralization activity of M39 antibody against

259   XBB.1.5 and JN.1 SARS-CoV-2 variants.

260   Collectively, our structural data suggest that somatic hypermutation in both contact and non-

261   contact residues of M2 may have contributed to the development of affinity specifically

262   towards the NTD of XBB.1.5, while the germline sequence likely endowed M39 with a broad

263   binding breadth.

264

265   *V gene pairing analysis reveals that the IGHV4-39/IGLV3-1 pair is specific to XBB.1.5.*

266   To further investigate the connection between mAb composition and their binding and

267   functional results, we performed a V gene pairing analysis of our specific and cross-reactive

268   mAbs. We analyzed the heavy and light chain genes and found a prevalent usage of IGHV1-

269   69 and IGKV3-20. Although these genes did not pair with each other for the binding mAbs,

270   they formed other pairings capable of binding to all subunits and domains in the ancestral S

271   protein (Figure 5a) as well as all variants and their respective RBD domains (Figure 5b).

272   Following IGHV1-69, the IGHV3-30 gene was also frequently used, consistent with previous

273   studies on COVID-19 vaccination(*21, 22*) and infection(*23, 24*). Additionally, we identified

274   two pairs of heavy and light chain V genes previously reported in the literature. The IGHV1-

275   69/IGKV3-11 pair was used by a public clone that binds to S2, providing partial *in vivo*

276   protection(*25*), and IGHV1-69/IGKV2-28 was previously identified as an RBD binder(*26*),

277   though in our data, the mAb using this pair bound only to the full spike protein in ELISA

278   experiments (Fig. 5b). Finally, we found that the cross-reactive M39 shared the IGHV5-

279   51/IGKV1-5 V gene combination with an antibody previously identified in naive repertoires

280   of SARS-CoV-2 infected patients *(27)*.

281

282   DISCUSSION

283   Vaccination is the primary and most potent control strategy to prevent COVID-19 effectively

284   and has been proven to elicit robust and protective humoral immunity in humans *(28, 29)*.

285   However, SARS-CoV-2 continues to mutate rapidly, developing a wide range of variants

286   capable of immune escape and, thus, causing breakthrough infections(*30*). As of January

287   2024, CDC reported that the JN.1 lineage had become predominant (~69% of cases)(*31*),

288   with its subvariants KP.2, KP.3, and LB.1 now dominating different parts of the world. The

289   constant emergence of VOCs demands the steady development and administration of

290   updated vaccines; however, whether these vaccinations can generate functional and variant-

291   specific humoral responses remains unclear.

292

293   In our study, most of the antibodies from the mRNA group bound to ancestral spike, XBB.1.5

294   spike, and JN.1 spike, with only one of them being XBB.1.5-specific, suggesting that the

295   participants' prior antigenic experiences (besides vaccination, all three participants of the

296   mRNA vaccine group have had infections pre-vaccination) might have influenced their

297   capacity to generate variant-specific responses. As for the recombinant protein vaccine

298   group, none of the mAbs tested were XBB.1.5 specific. Another study that used antibody

299   depletion to assess cross-reactive responses against ancestral and Omicron SARS-CoV-2

300   variants in participants who have received both primary vaccination and two ancestral/BA.5

301   or XBB.1.5 matched boosters reported that those without a history of infections had little to

302   no variant-specific antibodies, which seems to be the case for our findings at the monoclonal

303   level for one of the participants*(32–35)*.

304   When designing a SARS-CoV-2 variant vaccine, it is essential to determine how previous

305   exposures to novel variants, such as Omicron, can help to overcome immune imprinting

306   induced by the primary vaccination series. A recent study demonstrated that a single SARS-

307   CoV-2 exposure is insufficient to overcome immune imprinting, as the neutralization of viral

308   variants remained significantly lower compared to the neutralization of the ancestral strain

309   following just one previous Omicron infection*(36)*. However, neutralizing antibody titers

310   against viral variants significantly increased following two Omicron infections. Nevertheless,

311   previous infections do not provide absolute protection from emerging SARS-CoV-2 variants,

312   as that study has shown a decrease in the neutralization capacity of sera from Omicron—

313   infected individuals against XBB.1.5 pseudovirus containing targeted escape mutations*(36)*.

314   In our study, one of the participants from the mRNA vaccine group had two prior Omicron

315   infections (Participant 3), and all of the *in vitro* neutralizing antibodies (5/5, 100%) came from

316   this participant. The participant's repertoire also includes an antibody that cross-neutralizes

317   XBB.1.5 and JN.1 (M39); however, although the neutralization capacity of M39 against JN.1

318   is 100 times higher than XBB.1.5 *in vitro* (IC$_{50}$: 0.006 for JN.1 and IC$_{50}$:1.119 for XBB.1.5), the

319   difference is not translated into *in vivo* protection, as 100% of the animals were protected

320   against XBB.1.5 and only 60% against JN.1 (survival). Previous studies have reported that

321   mAbs using the same heavy chain V-gene as M39 (IGHV5-51) also either specifically*(37)* or

322   broadly*(37–40)* neutralize Omicron sub-variants, including XBB. Participant 1, who also had

323   two previous infections (ancestral before primary immunization and Omicron), contributed

324   the only XBB.1.5 specific antibody (M2). This antibody's robust binding activity (minimal

325   binding concentration < 0.01µg/mL) also translated into robust functional capacity: 100% of

326   survival following murine challenge with XBB.1.5, confirming that experiencing infections

327   before immunization can influence antibody levels and performance*(41)*. Consistent with the

328   literature, IGHV1-69 and IGHV3-30 were the most frequently used V genes. These genes are

329   commonly found within the repertoires of vaccinated individuals with a history of infection,

330   as was the case for most of our participants (4/5; 80%)*(42, 43)*.

331   Structural epitope mapping allows us to understand the molecular bases for antibody

332   binding breadth and potentially to predict the location and nature of amino acid

333   substitutions in future viral variants that would facilitate viral immune escape. We defined

334   and analyzed the epitopes of two protective antibodies, M2 and M39, which bind distinct

335   domains on the viral spike – the former binds NTD and the latter RBD. Both mAbs were likely

336   elicited by the XBB.1.5 vaccination or recent infection since they bind the XBB.1.5 variant

337   but do not interact with the ancestral WA.1 spike even though the ELISA data demonstrated

338   some binding. M39 additionally possesses prospective breadth toward JN.1. We posit that

339   insertion 141a (alignment relative to XBB.1.5 sequence) in WA.1 is the main determinant for

340   M2 mAb failing to bind WA.1, and that extensive substitutions in JN.1, including Q142H,

341   F152S and R153G restrict M2 binding to the XBB.1.5 variant (Fig. S6a). Analysis of the M39

342   structure shows that it binds to RBD outside of the ACE2 binding site and independently of

343   the RBD up or down position, similar to other class 3 antibodies (Fig. S8) like S309 and

344   C135*(44, 45)*. Although all three antibodies engage a similar epitope involving the residues

345   439-442 alpha-helix, the interacting residues of the three mAbs on RBD are distinct. M39

346   and C135 share a relatively small interface area of 562 $Å^2$ and 524 $Å^2$, respectively, while

347   S309 occupies a larger area of 795 $Å^2$. The RBD K440 is the major residue interacting with

348   M39 which might explain the reduced binding of this antibody to the WA.1 variant contains

349   N440. The conservation of the epitope on XBB.1.5, JN.1 and other Omicron variants,

350   however, confers broad cross-reactivity of M39.

351 Across the assessed metrics, the mRNA vaccine-elicited antibodies were present in a higher

352 proportion and, thus, had a higher number of functionally efficient monoclonals. Overall, the

353 XBB.1.5 vaccine from either platform could not overcome immune imprinting given that

354 most of the antibodies were also ancestral-spike reactive.

355 Our study shows, at the molecular level, that monovalent, variant-specific vaccines can elicit

356 functional antibodies. It also demonstrates the need for studies that compare the functional

357 and genetic differences of human mAbs induced by immunizations with different vaccine

358 platforms.

359

360 *Limitations of the study*

361 Our study has limitations. Although we analyzed over 600 single cells and expressed 100

362 human mAbs, they spanned five participants. Therefore, we do not have the power to

363 compare individuals vaccinated with mRNA vaccines versus recombinant protein-based

364 vaccines. In addition, we found three antibodies that bound both to S2 and NTD, and we

365 have not been able to elucidate the molecular mechanism of this dual binding so far.

366
367
368 ## MATERIAL AND METHODS
369

370 *Research Participant Demographic and biospecimen*

371 Biospecimen used in this paper are sourced from two Institutional Review Board (IRB)

372 approved observational research study protocols [STUDY-16-01215/IRB-16-00971 and

373 STUDY-20-00442 /IRB-20-03374] that collect samples before and after viral antigen

374 exposure. Following collection, all specimens were coded for deidentification purposes.

375 Peripheral blood mononuclear cells (PBMCs) were isolated using density gradient

376 centrifugation of whole blood samples from participants and SepMate tubes (STEMCELL

377 Technologies, 85460). PBMCs isolated from the blood samples were stored in liquid

378 nitrogen until analysis. All study participants provided informed consent for participation in

379   research prior to data or sample collection. All human participants' research is reviewed and

380   approved by the Program for the Protection of Human Participants at the Icahn School of

381   Medicine at Mount Sinai. All human participants research is done in compliance with 45 CFR

382   46 DHHS regulations.

383   Biospecimen were collected from five participants following vaccination with mRNA (Pfizer

384   or Moderna) or protein-based (Novavax) vaccine. Sample collection was done between 6-7

385   days post XBB.1.5 vaccination and cryopreserved peripheral mononuclear cells were used

386   to sort for plasmablasts. The average age of the participant was 46 years old; 3/5 participants

387   were male and all participants ancestries were reported as White. For 4/5 participants, the

388   XBB.1.5 vaccine was the fifth SARS-CoV-2 vaccine dose. XBB.1.5 vaccination was the 6th

389   dose for one participant. 2/5 participants had a homogenous Pfizer mRNA vaccine series. All

390   participants had Pfizer as their primary vaccine type and all participants received at least one

391   bivalent vaccine booster dose. One participant had a SARS-CoV-2 infection prior to any

392   vaccinations. In total, the range of SARS-CoV-2 infections experienced by participants prior

393   to XBB.1.5 vaccination ranged from no infections to two infections.

394

395   *Plasmablast sorting*

396   PBMCs were thawed with a combination of warmed Roswell Park Memorial Institute (RPMI)

397   1640 medium w/ L-glutamine and 25 mM 2-(4-(2-hydroxyethyl)-1-piperazinyl)-ethanesulfonic

398   acid (HEPES) (Corning, catalog no. 10-041-CV), 10% fetal bovine serum (FBS) (Gemini Bio,

399   catalog no.100-106), and 500 units of Benzonase Nuclease HC (Millipore Sigma, 70664-3).

400   After thawing, PBMC were washed with FACS buffer (phosphate-buffered saline (PBS)

401   (Corning, 21-040-CV)) with 2% FBS), resuspended in PBS for counting and viability

402   assessment (Table S2), then added to 15mL conical tubes to prepare for staining. Cells were

403   stained with surface antibodies (Table S3) diluted in Brilliant Buffer (BD Biosciences, 566349)

404   for 30 minutes at 4 °C protected from light. Following incubation, cells were washed with

405   PBS and dead cells were stained using LIVE/DEAD Fixable Blue Stain Kit (ThermoFisher,

406   L23105) diluted 1:1000 in PBS and incubated for 15 minutes at room temperature protected

407   from light. Subsequently, cells were washed with FACS buffer and resuspended for sorting

408   using the AuroraCS. Analyses were performed using FlowJo V.10.9 and the gating strategy

409   used to sort plasmablasts is shown in Figure S7.

410   *Single-cell RNA sequencing library preparation*

411   Following the manufacturer's protocols, sorted plasmablasts were prepared with the

412   Chromium Next GEM Single Cell 5' Reagent Kit v2 (10x Genomics, 1000244), combined with

413   barcoded Gel Beads (10x Genomics, 1000267), and partitioned into Gel Beads-in-emulsion

414   (GEMs) using a Chromium X controller and the Chromium Next GEM Chip K Single Cell Kit

415   (10x Genomics, 1000286). Following GEM generation, the GEMs underwent reverse

416   transcription to produce cDNA containing an Illumina TruSeq Read 1 sequence, unique

417   molecular identifier (UMI), template switch oligo (TSO), and 10x barcode. The resulting

418   cDNA was then purified using Dynabeads MyOne SILANE (10x Genomics, 2000048) and

419   amplified with reagents from the Chromium Next GEM Single Cell 5' Reagent Kit v2 (10x

420   Genomics, 1000244) to facilitate B cell receptor (BCR) amplification using a BCR

421   Amplification Kit (10x Genomics, 1000253). Utilizing a Library Construction Kit (10x

422   Genomics, 1000190), the BCR transcripts subsequently went through fragmentation, end-

423   repair, A-tailing, adaptor ligation, and sample index PCR to generate V(D)J libraries

424   containing standard Illumina primers, P5 and P7, dual indices, i5 and i7, and an Illumina

425   TruSeq Read 2 sequence. Following cDNA amplification, BCR amplification, and library

426   construction, samples were purified using SRPIselect (Beckman Coulter, B23317) and

427   quantified on an Agilent Tape Station 4150. Prior to sequencing, the size (bp) of the V(D)J

428   libraries was quantified on an Agilent TapeStation 4150 using a D5000 ScreenTape and

429   Reagents (Agilent, 5067-5588, 5067-5589), while the concentration (ng/uL) was measured

430   on a Qubit 4 using a Qubit 1X dsDNA High Sensitivity (HS) Assay Kit (Invitrogen, Q33231).

431   The V(D)J libraries were then denatured and diluted using a MiSeq Reagent Kit v3 (150-

432   cycle) (Illumina, MS-102-3001) and sequenced on an Illumina MiSeq. Following sequencing,

433   FASTQ files were converted from raw BCL files using the Illumina Basespace platform and

434   processed for data analysis on the 10x Genomics Cloud.

435

436   *Bioinformatic analyses of BCR sequencing*

437   We used the Immcantation framework to analyze V(D)J data outputted from 10x Genomics

438   CellRanger. V, D, and J genes were assigned using IgBlast v1.20.0 followed by parsing the

439   output to the Adaptive Immune Receptor Repertoire (AIRR) Community Rearrangement

440   using Change-O v1.3.0. Cells with non-productive sequences, multiple heavy-chains, or only

441   light chains were removed. Among multiple light chains, the one with the highest number

442   of mapped reads was chosen. Cells with no light chain were also removed. Clonal groups

443   were defined using the hierarchicalClones() function from SCOPer package v.1.3.0*(46)*, which

444   clusters BCR sequences based on common IGHV gene annotations, IGHJ gene annotations,

445   and junction length. This function defines groups based on sequence similarity, using the

446   within-group junction Hamming distance by single linkage, previously determined by the

447   distToNearest() function, from the SHazaM package v.1.2.0*(47)*, and using a similar threshold

448   for the junction region. The threshold was manually selected as 0.15. Clonal groups were

449   additionally formatted using running formatClones from the Dowser package 2.0 *(48)*, and

450   identical sequences were collapsed.

451   We estimated clonal abundance and quantified B cell clonal diversity using the

452   estimateAbundance and alphaDiversity functions from the Alakazam package v.1.3.0*(47)*,

453   respectively. For alphaDiversity, we applied resampling strategies to account for variations

454   in sequencing depth by downsampling each sample to the same number of sequences, and

455   at least 50 B cells per participant and 500 repetitions was reported. This method measures

456   diversity as a smooth function of the parameter "q", which corresponds to the most common

457   diversity metrics in ecology, namely: species richness (q = 0), the Shannon-Weiner index (q

458   = 1), and the Simpson index (q = 2)*(49)*.

459 Somatic hypermutation was determined by first reconstructing germline V and J sequences

460 using CreateGermline.py from Change-O, with masked D segment on downstream analysis.

461 The total number of mutations (R/S mutations in CDRs or frameworks) was determined for

462 the V gene using observedMutations from SHazaM. V gene usage and amino acid properties

463 for the CDR3 region were calculated using, respectively, countGenes and

464 aminoAcidProperties from the Alakazam package.

465

466 *VH/VL selection for mAbs expression*

467 Ig V(D)J and C gene assignments for plasmablast BCR sequences were performed with

468 IgBLAST using the AssignGenes and ParseDb functions from Change-O. These were filtered

469 to include cells with unique VH and VL sequences. Among cells with multiple light chain

470 sequences, the light chain sequence with the highest number of reads was chosen. Clonal

471 expansion analysis was performed on the filtered sequences using the DefineClones function

472 from Change-O. Cells belonging to the same expanded clone had identical V and J gene

473 usages in both heavy and light chains, along with >90% similarity in the heavy chain

474 complementarity determining region 3 (CDR3) nucleotide sequence. VH/VL sequences for

475 mAb expression were selected using the following criteria: unique VH/VL sequences within

476 all the expanded clones for mRNA vaccinees and the most mutated sequences in each of

477 the top six (Participant 4) and top four (Participant 5) clonotypes for the protein group were

478 chosen. This is because the number of sequences was higher for the Protein group than the

479 mRNA group, from which we selected all expanded clones. In addition, expanded clones

480 with at least two identical sequences were also selected for both vaccine groups. The

481 definition of unique sequences used was VH/VL sequences that were not part of an

482 expanded clone and had a VH mutation frequency < 5% (to enrich for de novo B cells) and

483 unique VJ gene usages in each subject (mRNA) and both participants combined (protein-

484 based). We chose this SHM filter to enrich for de novo XBB.1.5 specific mAbs, as they are

485 likely to have lower SHM than cross-reactive mAbs. Three sequences from the mRNA group

486   (M13, 14, and 15) were chosen for mAbs for presenting similarity (identical V, D, and J genes

487   and higher than 70% identity in the CDR3 aa sequence) with antibodies from a COVID-19

488   antibodies database (CoV-AbDab) *(50)*.

489

490   *Monoclonal antibody (mAb) production*

491   Sequences from all participants were chosen for mAb expression based on clonal expansion

492   as described before. Variable heavy and light chain domains were reformatted to IgG1,

493   synthesized, and cloned into mammalian expression vector pTwist IgG1, IgL2, or IgK utilizing

494   the Twist Bioscience eCommerce portal. Plasmidial DNA of said vectors were then extracted

495   from E.coli using PureYield™ Plasmid Maxiprep System (Promega, A2393) followed by

496   transfections of HEK 293F and EXPI293 cells were carried out using the lipid-based Thermo

497   Fisher Expi293™ Expression System Kit (ThermoFisher, A14525) and performed according

498   to the manufacturer's protocol. Briefly, plasmidial DNA, ExpiFectamine and 25, 50, or 100mL

499   cell cultures were incubated at 37°C 8%CO_2 for 18-22 hours on a platform shaker at 125rpm.

500   Enhancers 1 and 2 were then added and incubated on a platform shaker at 125rpm at 37°C

501   8% CO_2 for an additional 5-6 days. Following incubation, cells were pelleted by

502   centrifugation, the culture medium was filtered (0.45μM) and mixed with protein A agarose

503   resin (Gold Biotechnology, St. Louis, USA, P-400-50) for 12 hours at 4°C on a rotary shaker.

504   On the next day, the mix was loaded into Poly-Prep chromatography columns (Bio-Rad

505   Laboratories, Inc., 7311550), IgG was eluted with glycine and immediately neutralized with

506   1M Tris pH 8 and 5M NaCl. Purified IgGs were pooled, concentrated, and stored at 4°C short

507   term or -80°C long term for later use.

508   *Monoclonal antibody enzyme-linked immunosorbent assays (ELISAs)*

509   Recombinant proteins were coated on Immulon 4 HBX 96-well plates (Thermo Scientific) in

510   50 μL per well at a concentration of 2 μg/mL overnight at 4°C. The following day, plates were

511   washed three times using PBS containing 0.1% Tween-20 (PBST; Fisher Scientific) and

512   blocked using PBST supplemented with 3% non-fat milk (Life Technologies). Monoclonal

513   antibodies were diluted to 30 µg/mL and then serially diluted 1:3 to a final concentration of

514   1.52×10^{-3} µg/mL in PBST supplemented with 1% non-fat milk (Life Technologies). Following

515   blocking, mAb dilutions were added to the plates and incubated for 1 hour at room

516   temperature. A total of 16 wells per plate were intentionally left blank to serve as a measure

517   of background. Plates were washed three times with PBST and 100 µL of mouse anti-human

518   IgG antibody conjugated to horseradish peroxidase (Sigma, A0293) diluted 1:3000 in 1%

519   non-fat milk PBST was added to each well. Following 1 hour of incubation at room

520   temperature, plates were again washed three times with PBST and developed via the

521   addition of 100 µL of o-phenylenediamine dihydrochloride (OPD; Sigma-Aldrich). Plates

522   were developed for 10 minutes at room temperature and then the reaction was stopped by

523   adding 50 µL 3 M hydrochloric acid (HCl, Fisher) and plates were read using a Synergy 4

524   (BioTek) plate reader at an optical density (OD) of 490 nanometers.

525

526   *Neutralization assays*

527   Vero E6 cells expressing transmembrane protease serine 2 (TMPRSS2, BPS Biosciences,

528   78081) were cultured in Dulbecco's modified Eagle medium (DMEM; Gibco) supplemented

529   with 10% fetal bovine serum (FBS), 1% minimum essential medium (MEM) amino acids

530   solution (Gibco ,11130051), 100 units/mL penicillin and 100 µg/mL streptomycin (Gibco,

531   15140122), and 3 µg/mL puromycin (InvivoGen, ant-pr), and 100 µg/mL normocin

532   (InvivoGen, ant-nr). Viral stocks were verified via sequencing and enumerated using the 50%

533   tissue culture infectious dose ($TCID_{50}$) method. Microneutralization assays were carried out

534   as previously described*(51)*. Briefly, Vero.E6 TMPRSS2 were seeded in 96-well tissue culture

535   plates (Corning, 3340) at a density of 1×10^4 cells per well. 24 hours later, mAbs were diluted

536   to a starting concentration of 30 µg/mL in 1x minimal essential medium (MEM, Gibco)

537   supplemented with 2% FBS and then serially diluted 1:3 to a final concentration of

538   0.041µg/mL. 80 µL of mAb dilution was then mixed with 80 µL of SARS-CoV-2 diluted to 10^4

539     $TCID_{50}$/mL and allowed to incubate at room temperature for 1 hour. After 1 hour, 120 µL of

540   the virus/mAb mixture was used to infect the cells for 1 hour. The inoculum was then

541   removed and replaced with 100 μL 1xMEM 2% FBS and 100 μL of antibody dilution. Cells

542   were incubated at 37°C in a 5% CO_2 incubator for 48 hours prior to fixation with 10%

543   paraformaldehyde (Polysciences) for 24 hours. Once fixed, the paraformaldehyde was

544   removed, and the cells were permeabilized via the addition of 100 μL PBS supplemented

545   with 0.1% Triton X-100 (Fisher). Cells were permeabilized at room temperature for 15

546   minutes, after which the 0.1% Triton X-100 was removed, and the cells were blocked via the

547   addition of 100 μL 3% non-fat milk (Life Technologies) diluted in PBS. Cells were then stained

548   for the presence of SARS-CoV-2 nucleoprotein using the mAb 17C7 as previously

549   described[51].

550

551   *In vivo studies*

552   Animal studies were conducted following Animal Care and Use Committee (IACUC)

553   guidelines, according to approved protocols reviewed by the Icahn School of Medicine at

554   Mount Sinai Institutional Animal Care and Use Committee (IACUC). The 50% lethal dose

555   (LD_{50}) was calculated for WA1/2020, XBB.1.5, and JN.1 by infecting 6–8-week-old hACE2-

556   K18 mice with serial dilutions of virus ranging from 10^5 to 5 plaque-forming units (PFU),

557   diluted in sterile PBS. For protection studies, mice were treated intraperitoneally with a 10

558   mg/kg dose of mAb, diluted in 100 μl sterile PBS. Two hours later, mice were anesthetized

559   with 0.15 mg/kg ketamine and 0.03 mg/kg xylazine diluted in water for injection (WFI, Gibco)

560   and intranasally infected with a $3xLD_{50}$ dose of SARS-CoV-2 WA1/2020, XBB.1.5, or JN.1

561   diluted in 50 μl sterile PBS. Mice were monitored for weight loss for 14 days post-infection

562   and any animals falling below the 25% weight loss cut-off were humanely euthanized. The

563   influenza A virus antibody, CR9114, was utilized as a negative control[52].

564

565

566

567 *Cryo-EM sample preparation and data collection*

568 SARS-CoV-2 XBB.1.5 HexaPro spike*(53)* was incubated with M2 or M39 Fabs, at 2 mg/mL

569 with a 1.5 molar excess of fragment antigen binding (Fab) for 20 minutes at room

570 temperature. Immediately before grid preparation, fluorinated octyl-maltoside was added to

571 the preformed complex at 0.02% wt/vol final concentration. Then, 3 µl aliquots were applied

572 to UltrAuFoil gold R1.2/1.3 grids and subsequently blotted for 6 seconds at blot force 0 at

573 22°C and 85% humidity, then plunge-frozen in liquid ethane using a Vitrobot Mark IV system

574 (ThermoFisher Scientific). Grids were imaged on a Titan Krios microscope operated at 300

575 kV, equipped with a 15eV energy filter, and a Gatan K3 Direct Electron Detector. 6,034 and

576 6,112 movies were collected for M2 and M39 antibodies, respectively, with a total dose of

577 49.883 e-/ Å2/s. Images were collected at a magnification of 105,000, corresponding to a

578 calibrated pixel size of 0.825 Å/pixel, with a defocus range from -0.6 to -2.5µm.

579

580 *Cryo-EM data processing*

581 M2 complex

582 Movies were aligned and dose weighted using patch motion correction implemented in

583 cryoSPARC v4.3.1. Contrast transfer function estimation was done in cryoSPARC v4.3.1*(54)*

584 using Patch CTF, and particles were picked with cryoSPARC's template picker. The picked

585 particles were extracted with a box size of 1024 pixels, with 4× binning, and subjected to a

586 2D classification. Selected particles underwent two more rounds of 2D classification. An initial

587 model, with two classes, was generated from 856,516 selected particles. The best class,

588 containing 663,608 particles, was selected for further processing. After one round of non-

589 uniform refinement, without imposed symmetry, the particles were subjected to 3D

590 classification with six classes. Four classes were picked for further processing which contained

591 481,202 particles in total. The particles were re-extracted with a box size of 1024 pixels,

592 binned 2x, and selected for further rounds of non-uniform refinement with local and global

593   CTF refinement, yielding the final global map at a nominal resolution of 2.04 Å. The protomer

594   with the best Fab volume was subjected to local refinement with a soft mask extended by 6

595   pixels and padded by 12 pixels encompassing the N-terminal domain (NTD) and Fab. Local

596   map resulted in 2.38 Å resolution. The complex underwent another round of 3D classification

597   from which particles from 3 out of 5 classes were merged and subjected to local refinement,

598   yielding a final local map at 2.37 Å. The two half-maps from the local refinement were used

599   for sharpening in DeepEMhancer(55). The reported resolutions are based on the gold-

600   standard Fourier shell correlation of 0.143 criterion.

601   M39 complex

602   Movies were aligned and dose-weighted using MotionCorr2. Contrast transfer function

603   estimation was done in cryoSPARC v4.3.1 using Patch CTF, and particles were picked with

604   cryoSPARC's blob picker. The picked particles were extracted with a box size of 512 pixels,

605   with 4× binning, and subjected to a 2D classification. Selected particles were then subjected

606   to a second round of 2D classification. An initial model was generated on the 1,193,025

607   selected particles with three classes. The best class, containing 801,085 particles, was

608   selected for further processing. After one round of non-uniform refinement, without imposed

609   symmetry, the particles were subjected to 3D classification with ten classes. Of these, the

610   best seven classes, containing 552,337 particles in total, were combined, re-extracted

611   without binning with a box size of 512 pixels, and selected for further rounds of non-uniform

612   refinement with local CTF refinement, yielding the final global map at a nominal resolution

613   of 2.25 Å. The protomer with the two best Fab volumes was subjected to local refinement

614   with a soft mask extended by 6 pixels and padded by 8 pixels encompassing the receptor

615   binding domain (RBD) and Fabs. This yielded the local map at 2.69 Å resolution. A second

616   round of local refinement was performed with a soft mask encompassing the RBD and one

617   best Fab. This yielded the final local map at 2.65 Å resolution. The two half-maps from the

618   local refinement were used for sharpening in DeepEMhancer. The reported resolutions are

619   based on the gold-standard Fourier shell correlation of 0.143 criterion.

620 *Model building and refinement*

621 The DeepEMhancer sharpened focused maps were used for model building. Models for both

622 M2 and M39 complexes were initially built using ModelAngelo*(56)* and then manually

623 adjusted using COOT*(57)*. N-linked glycans were built manually in COOT using the glyco

624 extension and their stereochemistry and fit to the map were validated with Privateer*(58)*. The

625 model was then refined in Phenix*(59)* using real-space refinement and validated with

626 MolProbity*(60)* (See Table S4). The structural biology software was compiled and distributed

627 by SBGrid*(61)*.

628

629 **Statistical Analysis**

630 Statistical tests were performed in Prism 10 (GraphPad Software, La Jolla, CA, USA) or R

631 (version 4.2.1, The R Foundation for Statistical Computing). Comparisons between vaccine

632 groups (mRNA vs protein) were performed using unpaired Mann-Whitney's test, as also

633 indicated in the figure legends. Only significant test results are shown in the figures and the

634 P-values are defined as follows: $p \leq 0.05$: *; $p \leq 0.01$: **; $p \leq 0.001$: ***; $p \leq 0.0001$: ****.

635 The area under the curve (AUC) and minimal binding concentrations were calculated using

636 the average OD plus 5x standard deviation of the blank wells.

637

638

639

640

641

642

643

644

645

646   SUPPLEMENTAL INFORMATION

647   Fig. S1 – S8

648   Tables S1 – S4

649   References 45, 62 – 63.

650

651

652

653

654

655

656

657

658

659

660

661

662

663

664

665

666

667

668

669

670

671

672

REFERENCES

1. Y. Yang, L. Du, SARS-CoV-2 spike protein: a key target for eliciting persistent neutralizing antibodies., *Signal Transduct. Target. Ther.* **6**, 95 (2021).

2. S. J. Zost, P. Gilchuk, J. B. Case, E. Binshtein, R. E. Chen, J. P. Nkolola, A. Schäfer, J. X. Reidy, A. Trivette, R. S. Nargi, R. E. Sutton, N. Suryadevara, D. R. Martinez, L. E. Williamson, E. C. Chen, T. Jones, S. Day, L. Myers, A. O. Hassan, N. M. Kafai, J. E. Crowe, Potently neutralizing and protective human antibodies against SARS-CoV-2., *Nature* **584**, 443–449 (2020).

3. E. Cameroni, J. E. Bowen, L. E. Rosen, C. Saliba, S. K. Zepeda, K. Culap, D. Pinto, L. A. VanBlargan, A. De Marco, J. di Iulio, F. Zatta, H. Kaiser, J. Noack, N. Farhat, N. Czudnochowski, C. Havenar-Daughton, K. R. Sprouse, J. R. Dillen, A. E. Powell, A. Chen, D. Corti, Broadly neutralizing antibodies overcome SARS-CoV-2 Omicron antigenic shift., *Nature* **602**, 664–670 (2022).

4. R. E. Chen, E. S. Winkler, J. B. Case, I. D. Aziati, T. L. Bricker, A. Joshi, T. L. Darling, B. Ying, J. M. Errico, S. Shrihari, L. A. VanBlargan, X. Xie, P. Gilchuk, S. J. Zost, L. Droit, Z. Liu, S. Stumpf, D. Wang, S. A. Handley, W. B. Stine, M. S. Diamond, In vivo monoclonal antibody efficacy against SARS-CoV-2 variant strains., *Nature* **596**, 103–108 (2021).

5. W. B. Alsoussi, S. K. Malladi, J. Q. Zhou, Z. Liu, B. Ying, W. Kim, A. J. Schmitz, T. Lei, S. C. Horvath, A. J. Sturtz, K. M. McIntire, B. Evavold, F. Han, S. M. Scheaffer, I. F. Fox, S. F. Mirza, L. Parra-Rodriguez, R. Nachbagauer, B. Nestorova, S. Chalkias, A. H. Ellebedy, SARS-CoV-2 Omicron boosting induces de novo B cell response in humans., *Nature* **617**, 592–598 (2023).

6. J. Guenthoer, M. Lilly, T. N. Starr, B. Dadonaite, K. N. Lovendahl, J. T. Croft, C. I. Stoddard, V. Chohan, S. Ding, F. Ruiz, M. S. Kopp, A. Finzi, J. D. Bloom, H. Y. Chu, K. K. Lee, J. Overbaugh, Identification of broad, potent antibodies to functionally constrained regions of SARS-CoV-2 spike following a breakthrough infection., *Proc Natl Acad Sci USA* **120**, e2220948120 (2023).

7. T. N. Starr, N. Czudnochowski, Z. Liu, F. Zatta, Y.-J. Park, A. Addetia, D. Pinto, M. Beltramello, P. Hernandez, A. J. Greaney, R. Marzi, W. G. Glass, I. Zhang, A. S. Dingens, J. E. Bowen, M. A. Tortorici, A. C. Walls, J. A. Wojcechowskyj, A. De Marco, L. E. Rosen, G. Snell, SARS-CoV-2 RBD antibodies that maximize breadth and resistance to escape., *Nature* **597**, 97–102 (2021).

8. J. L. Torres, G. Ozorowski, E. Andreano, H. Liu, J. Copps, G. Piccini, L. Donnici, M. Conti,

706   C. Planchais, D. Planas, N. Manganaro, E. Pantano, I. Paciello, P. Pileri, T. Bruel, E.
707   Montomoli, H. Mouquet, O. Schwartz, C. Sala, R. De Francesco, A. B. Ward, Structural
708   insights of a highly potent pan-neutralizing SARS-CoV-2 human monoclonal antibody., *Proc*
709   *Natl Acad Sci USA* **119**, e2120976119 (2022).

710   9. N. Andrews, J. Stowe, F. Kirsebom, S. Toffa, T. Rickeard, E. Gallagher, C. Gower, M. Kall,
711   N. Groves, A.-M. O'Connell, D. Simons, P. B. Blomquist, A. Zaidi, S. Nash, N. Iwani Binti
712   Abdul Aziz, S. Thelwall, G. Dabrera, R. Myers, G. Amirthalingam, S. Gharbia, J. Lopez Bernal,
713   Covid-19 Vaccine Effectiveness against the Omicron (B.1.1.529) Variant., *N. Engl. J. Med.*
714   **386**, 1532–1546 (2022).

715   10. Y. Cao, J. Wang, F. Jian, T. Xiao, W. Song, A. Yisimayi, W. Huang, Q. Li, P. Wang, R. An,
716   J. Wang, Y. Wang, X. Niu, S. Yang, H. Liang, H. Sun, T. Li, Y. Yu, Q. Cui, S. Liu, X. S. Xie,
717   Omicron escapes the majority of existing SARS-CoV-2 neutralizing antibodies., *Nature* **602**,
718   657–663 (2022).

719   11. S. Cele, L. Jackson, D. S. Khoury, K. Khan, T. Moyo-Gwete, H. Tegally, J. E. San, D.
720   Cromer, C. Scheepers, D. G. Amoako, F. Karim, M. Bernstein, G. Lustig, D. Archary, M.
721   Smith, Y. Ganga, Z. Jule, K. Reedoy, S.-H. Hwa, J. Giandhari, A. Sigal, Omicron extensively
722   but incompletely escapes Pfizer BNT162b2 neutralization., *Nature* **602**, 654–656 (2022).

723   12. A. Aggarwal, A. Akerman, V. Milogiannakis, M. R. Silva, G. Walker, A. O. Stella, A.
724   Kindinger, T. Angelovich, E. Waring, S. Amatayakul-Chantler, N. Roth, S. Manni, T. Hauser,
725   T. Barnes, A. Condylios, M. Yeang, M. Wong, T. Jean, C. S. P. Foster, D. Christ, S. G. Turville,
726   SARS-CoV-2 Omicron BA.5: Evolving tropism and evasion of potent humoral responses and
727   resistance to clinical immunotherapeutics relative to viral variants of concern., *EBioMedicine*
728   **84**, 104270 (2022).

729   13. W. Dejnirattisai, R. H. Shaw, P. Supasa, C. Liu, A. S. Stuart, A. J. Pollard, X. Liu, T. Lambe,
730   D. Crook, D. I. Stuart, J. Mongkolsapaya, J. S. Nguyen-Van-Tam, M. D. Snape, G. R.
731   Screaton, Com-COV2 study group, Reduced neutralisation of SARS-CoV-2 omicron
732   B.1.1.529 variant by post-immunisation serum., *Lancet* **399**, 234–236 (2022).

733   14. L. Liu, S. Iketani, Y. Guo, J. F.-W. Chan, M. Wang, L. Liu, Y. Luo, H. Chu, Y. Huang, M. S.
734   Nair, J. Yu, K. K.-H. Chik, T. T.-T. Yuen, C. Yoon, K. K.-W. To, H. Chen, M. T. Yin, M. E.
735   Sobieszczyk, Y. Huang, H. H. Wang, D. D. Ho, Striking antibody evasion manifested by the
736   Omicron variant of SARS-CoV-2, *Nature* (2021), doi:10.1038/d41586-021-03826-3.

737   15. W. F. Garcia-Beltran, K. J. St Denis, A. Hoelzemer, E. C. Lam, A. D. Nitido, M. L. Sheehan,
738   C. Berrios, O. Ofoman, C. C. Chang, B. M. Hauser, J. Feldman, A. L. Roederer, D. J. Gregory,

739   M. C. Poznansky, A. G. Schmidt, A. J. Iafrate, V. Naranbhai, A. B. Balazs, mRNA-based
740   COVID-19 vaccine boosters induce neutralizing immunity against SARS-CoV-2 Omicron
741   variant., *Cell* **185**, 457-466.e4 (2022).

742   16. P. Qu, J. N. Faraone, J. P. Evans, Y.-M. Zheng, C. Carlin, M. Anghelina, P. Stevens, S.
743   Fernandez, D. Jones, A. R. Panchal, L. J. Saif, E. M. Oltz, B. Zhang, T. Zhou, K. Xu, R. J.
744   Gumina, S.-L. Liu, Enhanced evasion of neutralizing antibody response by Omicron XBB.1.5,
745   CH.1.1, and CA.3.1 variants., *Cell Rep.* **42**, 112443 (2023).

746   17. Q. Wang, Y. Guo, S. Iketani, M. S. Nair, Z. Li, H. Mohri, M. Wang, J. Yu, A. D. Bowen, J.
747   Y. Chang, J. G. Shah, N. Nguyen, Z. Chen, K. Meyers, M. T. Yin, M. E. Sobieszczyk, Z. Sheng,
748   Y. Huang, L. Liu, D. D. Ho, Antibody evasion by SARS-CoV-2 Omicron subvariants BA.2.12.1,
749   BA.4 and BA.5., *Nature* **608**, 603–608 (2022).

750   18. Food & Drug Administration, Novavax COVID-19 Vaccine, Adjuvanted (2023) (available
751   at   https://www.fda.gov/vaccines-blood-biologics/coronavirus-covid-19-cber-regulated-
752   biologics/novavax-covid-19-vaccine-adjuvanted).

753   19.   Unable to find information for 16609429.

754   20. E. S. Winkler, A. L. Bailey, N. M. Kafai, S. Nair, B. T. McCune, J. Yu, J. M. Fox, R. E. Chen,
755   J. T. Earnest, S. P. Keeler, J. H. Ritter, L.-I. Kang, S. Dort, A. Robichaud, R. Head, M. J.
756   Holtzman, M. S. Diamond, SARS-CoV-2 infection of human ACE2-transgenic mice causes
757   severe lung inflammation and impaired function., *Nat. Immunol.* **21**, 1327–1335 (2020).

758   21. Y. Wang, M. Yuan, H. Lv, J. Peng, I. A. Wilson, N. C. Wu, A large-scale systematic survey
759   reveals recurring molecular features of public antibody responses to SARS-CoV-2., *Immunity*
760   **55**, 1105-1117.e4 (2022).

761   22. E. Andreano, I. Paciello, G. Pierleoni, G. Piccini, V. Abbiento, G. Antonelli, P. Pileri, N.
762   Manganaro, E. Pantano, G. Maccari, S. Marchese, L. Donnici, L. Benincasa, G. Giglioli, M.
763   Leonardi, C. De Santi, M. Fabbiani, I. Rancan, M. Tumbarello, F. Montagnani, R. Rappuoli, B
764   cell analyses after SARS-CoV-2 mRNA third vaccination reveals a hybrid immunity like
765   antibody response., *Nat. Commun.* **14**, 53 (2023).

766   23. M. Claireaux, T. G. Caniels, M. de Gast, J. Han, D. Guerra, G. Kerster, B. D. C. van Schaik,
767   A. Jongejan, A. I. Schriek, M. Grobben, P. J. M. Brouwer, K. van der Straten, Y. Aldon, J.
768   Capella-Pujol, J. L. Snitselaar, W. Olijhoek, A. Aartse, M. Brinkkemper, I. Bontjer, J. A.
769   Burger, M. J. van Gils, A public antibody class recognizes an S2 epitope exposed on open
770   conformations of SARS-CoV-2 spike., *Nat. Commun.* **13**, 4539 (2022).

771   24. P. Pushparaj, A. Nicoletto, X. C. Dopico, D. J. Sheward, S. Kim, S. Ekström, B. Murrell,

772 M. Corcoran, G. B. Karlsson Hedestam, Frequent use of IGHV3-30-3 in SARS-CoV-2
773 neutralizing antibody responses., *Front. Virol.* **3**, 1128253 (2023).

774 25. T. J. C. Tan, A. K. Verma, A. Odle, R. Lei, D. K. Meyerholz, K. A. Matreyek, S. Perlman,
775 L.-Y. R. Wong, N. C. Wu, Evidence of antigenic drift in the fusion machinery core of SARS-
776 CoV-2 spike., *Proc Natl Acad Sci USA* **121**, e2317222121 (2024).

777 26. E. Rujas, I. Kucharska, Y. Z. Tan, S. Benlekbir, H. Cui, T. Zhao, G. A. Wasney, P.
778 Budylowski, F. Guvenc, J. C. Newton, T. Sicard, A. Semesi, K. Muthuraman, A.
779 Nouanesengsy, C. B. Aschner, K. Prieto, S. A. Bueler, S. Youssef, S. Liao-Chan, J. Glanville,
780 J.-P. Julien, Multivalency transforms SARS-CoV-2 antibodies into ultrapotent neutralizers.,
781 *Nat. Commun.* **12**, 3661 (2021).

782 27. B. N. Bell, A. E. Powell, C. Rodriguez, J. R. Cochran, P. S. Kim, Neutralizing antibodies
783 targeting the SARS-CoV-2 receptor binding domain isolated from a naïve human antibody
784 library., *Protein Sci.* **30**, 716–727 (2021).

785 28. F. P. Polack, S. J. Thomas, N. Kitchin, J. Absalon, A. Gurtman, S. Lockhart, J. L. Perez, G.
786 Pérez Marc, E. D. Moreira, C. Zerbini, R. Bailey, K. A. Swanson, S. Roychoudhury, K. Koury,
787 P. Li, W. V. Kalina, D. Cooper, R. W. Frenck, L. L. Hammitt, Ö. Türeci, C4591001 Clinical Trial
788 Group, Safety and Efficacy of the BNT162b2 mRNA Covid-19 Vaccine., *N. Engl. J. Med.* **383**,
789 2603–2615 (2020).

790 29. Z. Zhang, J. Mateus, C. H. Coelho, J. M. Dan, C. R. Moderbacher, R. I. Gálvez, F. H.
791 Cortes, A. Grifoni, A. Tarke, J. Chang, E. A. Escarrega, C. Kim, B. Goodwin, N. I. Bloom, A.
792 Frazier, D. Weiskopf, A. Sette, S. Crotty, Humoral and cellular immune memory to four
793 COVID-19 vaccines., *Cell* **185**, 2434-2451.e17 (2022).

794 30. A. M. Carabelli, T. P. Peacock, L. G. Thorne, W. T. Harvey, J. Hughes, COVID-19
795 Genomics UK Consortium, S. J. Peacock, W. S. Barclay, T. I. de Silva, G. J. Towers, D. L.
796 Robertson, SARS-CoV-2 variant biology: immune escape, transmission and fitness., *Nat. Rev.*
797 *Microbiol.* **21**, 162–177 (2023).

798 31. C D C, Early Estimates of Updated 2023–2024 (Monovalent XBB.1.5) COVID-19 Vaccine
799 Effectiveness Against Symptomatic SARS-CoV-2 Infection Attributable to Co-Circulating
800 Omicron Variants Among Immunocompetent Adults — Increasing Community Access to
801 Testing Program, United States, September 2023–January 2024 (2024) (available at
802 https://www.cdc.gov/mmwr/volumes/73/wr/mm7304a2.htm#:~:text=On%20September%2
803 012%2C%202023%2C%20CDC's,-19%2C%20including%20severe%20disease.).

804 32. C.-Y. Liang, S. Raju, Z. Liu, Y. Li, G. A. Arunkumar, J. B. Case, S. J. Zost, C. M. Acreman,

D. C. Carvalho dos Anjos, J. S. McLellan, J. E. Crowe, S. P. J. Whelan, S. M. Elbashir, D. K. Edwards, M. S. Diamond, Prototype mRNA vaccines imprint broadly neutralizing human serum antibodies after Omicron variant-matched boosting, *BioRxiv* (2024), doi:10.1101/2024.01.03.574018.

33. J. M. Carreño, G. Singh, V. Simon, F. Krammer, PVI study group, Bivalent COVID-19 booster vaccines and the absence of BA.5-specific antibodies., *Lancet Microbe* **4**, e569 (2023).

34. F. Krammer, A. H. Ellebedy, Variant-adapted COVID-19 booster vaccines., *Science* **382**, 157–159 (2023).

35. M. A. Tortorici, A. Addetia, A. J. Seo, J. Brown, K. Sprouse, J. Logue, E. Clark, N. Franko, H. Chu, D. Veesler, Persistent immune imprinting occurs after vaccination with the COVID-19 XBB.1.5 mRNA booster in humans., *Immunity* **57**, 904-911.e4 (2024).

36. A. Yisimayi, W. Song, J. Wang, F. Jian, Y. Yu, X. Chen, Y. Xu, S. Yang, X. Niu, T. Xiao, J. Wang, L. Zhao, H. Sun, R. An, N. Zhang, Y. Wang, P. Wang, L. Yu, Z. Lv, Q. Gu, Y. Cao, Repeated Omicron exposures override ancestral SARS-CoV-2 immune imprinting., *Nature* **625**, 148–156 (2024).

37. Y. Cao, F. Jian, J. Wang, Y. Yu, W. Song, A. Yisimayi, J. Wang, R. An, X. Chen, N. Zhang, Y. Wang, P. Wang, L. Zhao, H. Sun, L. Yu, S. Yang, X. Niu, T. Xiao, Q. Gu, F. Shao, X. S. Xie, Imprinted SARS-CoV-2 humoral immunity induces convergent Omicron RBD evolution., *Nature* **614**, 521–529 (2023).

38. J. Seow, Z. A. Shalim, C. Graham, S. Kimuda, A. Pillai, T. Lechmere, A. Kurshan, A. M. Khimji, L. B. Snell, G. Nebbia, C. Mant, A. Waters, J. Fox, M. H. Malim, K. J. Doores, Broad and potent neutralizing mAbs are elicited in vaccinated individuals following Delta/BA.1 breakthrough infection, *BioRxiv* (2023), doi:10.1101/2023.03.30.534872.

39. Y. Cao, A. Yisimayi, F. Jian, W. Song, T. Xiao, L. Wang, S. Du, J. Wang, Q. Li, X. Chen, Y. Yu, P. Wang, Z. Zhang, P. Liu, R. An, X. Hao, Y. Wang, J. Wang, R. Feng, H. Sun, X. S. Xie, BA.2.12.1, BA.4 and BA.5 escape antibodies elicited by Omicron infection., *Nature* **608**, 593–602 (2022).

40. W.-T. He, R. Musharrafieh, G. Song, K. Dueker, L. V. Tse, D. R. Martinez, A. Schäfer, S. Callaghan, P. Yong, N. Beutler, J. L. Torres, R. M. Volk, P. Zhou, M. Yuan, H. Liu, F. Anzanello, T. Capozzola, M. Parren, E. Garcia, S. A. Rawlings, R. Andrabi, Targeted isolation of panels of diverse human protective broadly neutralizing antibodies against SARS-like viruses., *BioRxiv* (2022), doi:10.1101/2021.09.08.459480.

41. K. Srivastava, J. M. Carreño, C. Gleason, B. Monahan, G. Singh, A. Abbad, J. Tcheou, A. Raskin, G. Kleiner, H. van Bakel, E. M. Sordillo, PARIS Study Group, F. Krammer, V. Simon, SARS-CoV-2-infection- and vaccine-induced antibody responses are long lasting with an initial waning phase followed by a stabilization phase., *Immunity* **57**, 587-599.e4 (2024).

42. E. Andreano, I. Paciello, G. Piccini, N. Manganaro, P. Pileri, I. Hyseni, M. Leonardi, E. Pantano, V. Abbiento, L. Benincasa, G. Giglioli, C. De Santi, M. Fabbiani, I. Rancan, M. Tumbarello, F. Montagnani, C. Sala, E. Montomoli, R. Rappuoli, Hybrid immunity improves B cells and antibodies against SARS-CoV-2 variants., *Nature* **600**, 530–535 (2021).

43. M. Chernyshev, M. Sakharkar, R. I. Connor, H. L. Dugan, D. J. Sheward, C. G. Rappazzo, A. Stålmarck, M. N. E. Forsell, P. F. Wright, M. Corcoran, B. Murrell, L. M. Walker, G. B. Karlsson Hedestam, Vaccination of SARS-CoV-2-infected individuals expands a broad range of clonally diverse affinity-matured B cell lineages., *Nat. Commun.* **14**, 2249 (2023).

44. D. Pinto, Y.-J. Park, M. Beltramello, A. C. Walls, M. A. Tortorici, S. Bianchi, S. Jaconi, K. Culap, F. Zatta, A. De Marco, A. Peter, B. Guarino, R. Spreafico, E. Cameroni, J. B. Case, R. E. Chen, C. Havenar-Daughton, G. Snell, A. Telenti, H. W. Virgin, D. Corti, Cross-neutralization of SARS-CoV-2 by a human monoclonal SARS-CoV antibody., *Nature* **583**, 290–295 (2020).

45. C. O. Barnes, C. A. Jette, M. E. Abernathy, K.-M. A. Dam, S. R. Esswein, H. B. Gristick, A. G. Malyutin, N. G. Sharaf, K. E. Huey-Tubman, Y. E. Lee, D. F. Robbiani, M. C. Nussenzweig, A. P. West, P. J. Bjorkman, SARS-CoV-2 neutralizing antibody structures inform therapeutic strategies., *Nature* **588**, 682–687 (2020).

46. N. Nouri, S. H. Kleinstein, Somatic hypermutation analysis for improved identification of B cell clonal families from next-generation sequencing data., *PLoS Comput. Biol.* **16**, e1007977 (2020).

47. N. T. Gupta, J. A. Vander Heiden, M. Uduman, D. Gadala-Maria, G. Yaari, S. H. Kleinstein, Change-O: a toolkit for analyzing large-scale B cell immunoglobulin repertoire sequencing data., *Bioinformatics* **31**, 3356–3358 (2015).

48. K. B. Hoehn, O. G. Pybus, S. H. Kleinstein, Phylogenetic analysis of migration, differentiation, and class switching in B cells., *PLoS Comput. Biol.* **18**, e1009885 (2022).

49. M. O. Hill, Diversity and Evenness: A Unifying Notation and Its Consequences, *Ecology* **54**, 427–432 (1973).

50. M. I. J. Raybould, C. Marks, A. Kovaltsuk, A. P. Lewis, J. Shi, C. M. Deane, Public Baseline and shared response structures support the theory of antibody repertoire functional

871   commonality., *PLoS Comput. Biol.* **17**, e1008781 (2021).

872   51. J. M. Carreño, H. Alshammary, J. Tcheou, G. Singh, A. J. Raskin, H. Kawabata, L. A.
873   Sominsky, J. J. Clark, D. C. Adelsberg, D. A. Bielak, A. S. Gonzalez-Reiche, N. Dambrauskas,
874   V. Vigdorovich, PSP-PARIS Study Group, K. Srivastava, D. N. Sather, E. M. Sordillo, G. Bajic,
875   H. van Bakel, V. Simon, F. Krammer, Activity of convalescent and vaccine serum against
876   SARS-CoV-2 Omicron., *Nature* **602**, 682–688 (2022).

877   52. C. Dreyfus, N. S. Laursen, T. Kwaks, D. Zuijdgeest, R. Khayat, D. C. Ekiert, J. H. Lee, Z.
878   Metlagel, M. V. Bujny, M. Jongeneelen, R. van der Vlugt, M. Lamrani, H. J. W. M. Korse, E.
879   Geelen, Ö. Sahin, M. Sieuwerts, J. P. J. Brakenhoff, R. Vogels, O. T. W. Li, L. L. M. Poon, R.
880   H. E. Friesen, Highly conserved protective epitopes on influenza B viruses., *Science* **337**,
881   1343–1348 (2012).

882   53. C.-L. Hsieh, J. A. Goldsmith, J. M. Schaub, A. M. DiVenere, H.-C. Kuo, K. Javanmardi, K.
883   C. Le, D. Wrapp, A. G. Lee, Y. Liu, C.-W. Chou, P. O. Byrne, C. K. Hjorth, N. V. Johnson, J.
884   Ludes-Meyers, A. W. Nguyen, J. Park, N. Wang, D. Amengor, J. J. Lavinder, J. S. McLellan,
885   Structure-based design of prefusion-stabilized SARS-CoV-2 spikes., *Science* **369**, 1501–1505
886   (2020).

887   54. A. Punjani, J. L. Rubinstein, D. J. Fleet, M. A. Brubaker, cryoSPARC: algorithms for rapid
888   unsupervised cryo-EM structure determination., *Nat. Methods* **14**, 290–296 (2017).

889   55. R. Sanchez-Garcia, J. Gomez-Blanco, A. Cuervo, J. M. Carazo, C. O. S. Sorzano, J.
890   Vargas, DeepEMhancer: a deep learning solution for cryo-EM volume post-processing.,
891   *Commun. Biol.* **4**, 874 (2021).

892   56. K. Jamali, L. Käll, R. Zhang, A. Brown, D. Kimanius, S. H. W. Scheres, Automated model
893   building and protein identification in cryo-EM maps., *Nature* **628**, 450–457 (2024).

894   57. P. Emsley, B. Lohkamp, W. G. Scott, K. Cowtan, Features and development of Coot.,
895   *Acta Crystallogr. D Biol. Crystallogr.* **66**, 486–501 (2010).

896   58. J. Agirre, J. Iglesias-Fernández, C. Rovira, G. J. Davies, K. S. Wilson, K. D. Cowtan,
897   Privateer: software for the conformational validation of carbohydrate structures., *Nat. Struct.*
898   *Mol. Biol.* **22**, 833–834 (2015).

899   59. D. Liebschner, P. V. Afonine, M. L. Baker, G. Bunkóczi, V. B. Chen, T. I. Croll, B. Hintze,
900   L. W. Hung, S. Jain, A. J. McCoy, N. W. Moriarty, R. D. Oeffner, B. K. Poon, M. G. Prisant, R.
901   J. Read, J. S. Richardson, D. C. Richardson, M. D. Sammito, O. V. Sobolev, D. H. Stockwell,
902   P. D. Adams, Macromolecular structure determination using X-rays, neutrons and electrons:
903   recent developments in Phenix., *Acta Crystallogr. D Struct. Biol.* **75**, 861–877 (2019).

904   60. C. J. Williams, J. J. Headd, N. W. Moriarty, M. G. Prisant, L. L. Videau, L. N. Deis, V.
905   Verma, D. A. Keedy, B. J. Hintze, V. B. Chen, S. Jain, S. M. Lewis, W. B. Arendall, J. Snoeyink,
906   P. D. Adams, S. C. Lovell, J. S. Richardson, D. C. Richardson, MolProbity: more and better
907   reference data for improved all-atom structure validation., *Protein Sci.* **27**, 293–315 (2018).

908   61. A. Morin, B. Eisenbraun, J. Key, P. C. Sanschagrin, M. A. Timony, M. Ottaviano, P. Sliz,
909   Collaboration gets the most out of software., *eLife* **2**, e01456 (2013).

910   62. K. E. Atanasoff, L. Brambilla, D. C. Adelsberg, S. Kowdle, C. S. Stevens, S. Slamanig, C.-
911   T. Hung, Y. Fu, R. Lim, L. Tran, R. Allen, W. Sun, J. A. Duty, G. Bajic, B. Lee, D. Tortorella,
912   An in vitro experimental pipeline to characterize the epitope of a SARS-CoV-2 neutralizing
913   antibody., *MBio* **15**, e0247723 (2024).

914   63. J. Huo, Y. Zhao, J. Ren, D. Zhou, H. M. E. Duyvesteyn, H. M. Ginn, L. Carrique, T.
915   Malinauskas, R. R. Ruza, P. N. M. Shah, T. K. Tan, P. Rijal, N. Coombes, K. R. Bewley, J. A.
916   Tree, J. Radecke, N. G. Paterson, P. Supasa, J. Mongkolsapaya, G. R. Screaton, D. I. Stuart,
917   Neutralization of SARS-CoV-2 by Destruction of the Prefusion Spike., *Cell Host Microbe* **28**,
918   445-454.e6 (2020).

919

920

ACKNOWLEDGMENTS

929

FUNDING

944

945

Author Contributions

947   CHC, FK and VS conceptualized the study. RFF, JCC, HC, DJ, BB, AC, JY, RAS, JN, KS, and

948   KB conducted the experiments. RFF, JCC, HC, DJ, VR, BB, IL, GB, FK, VS and CHC analyzed

949   the data. GB, FK, VS, and CHC supervised and funded the study. VS, KS, and JN provided

950   access to biospecimen and metadata from study participants. EL and SK supervised

951   bioinformatic analyses. GB, FK, VS, and CHC were responsible for the decision to submit the

952   manuscript for publication. RFF, JJC, HC, DJ, IL, VR, GB and CHC wrote the manuscript. All

953   authors interpreted the data, provided critical input, and revised the manuscript.

954

## Competing interests

956   The Icahn School of Medicine at Mount Sinai has filed patent applications relating to SARS-

957   CoV-2 serological assays, NDV-based SARS-CoV-2 vaccines influenza virus vaccines and

958   influenza virus therapeutics which list Florian Krammer as co-inventor. Viviana Simon is listed

959   on the SARS-CoV-2 serological assay patent application as co-inventor. Mount Sinai has spun

960   out a company, Kantaro, to market serological tests for SARS-CoV-2 and another company,

961 CastleVax, to develop SARS-CoV-2 vaccines. Florian Krammer is co-founder and scientific

962 advisory board member of CastleVax. Florian Krammer has consulted for Merck, Curevac,

963 GSK, Seqirus and Pfizer and is currently consulting for 3rd Rock Ventures, Gritstone and

964 Avimex. The Krammer laboratory is collaborating with Dynavax on influenza vaccine

965 development and with VIR on influenza virus therapeutics.

966

967 ## Data Availability

968 Deidentified data may be made available to investigators whose proposed use of the data

969 has been approved by the Icahn School of Medicine Ethics Review Board upon request to

970 the corresponding authors. Participants' metadata have been deposited to BioProject

971 accession number PRJNA1134144 in the NCBI BioProject database.The EM maps have been

972 deposited in the Electron Microscopy Data Bank (EMDB) under accession codes EMD-45443

973 and EMD-45444 for the M39 and M2 complexes, respectively. The accompanying atomic

974 coordinates have been deposited in the Protein Data Bank (PDB) under accession codes

975 9CCI and 9CCJ for the M39 and M2 complexes, respectively. The aligned micrographs are

976 available on the Electron Microscopy Public Image Archive (EMPIAR) under accession

977 numbers EMPIAR-12167 and EMPIAR-12151.

978

979

980

981

982

983

984

985

986   FIGURES
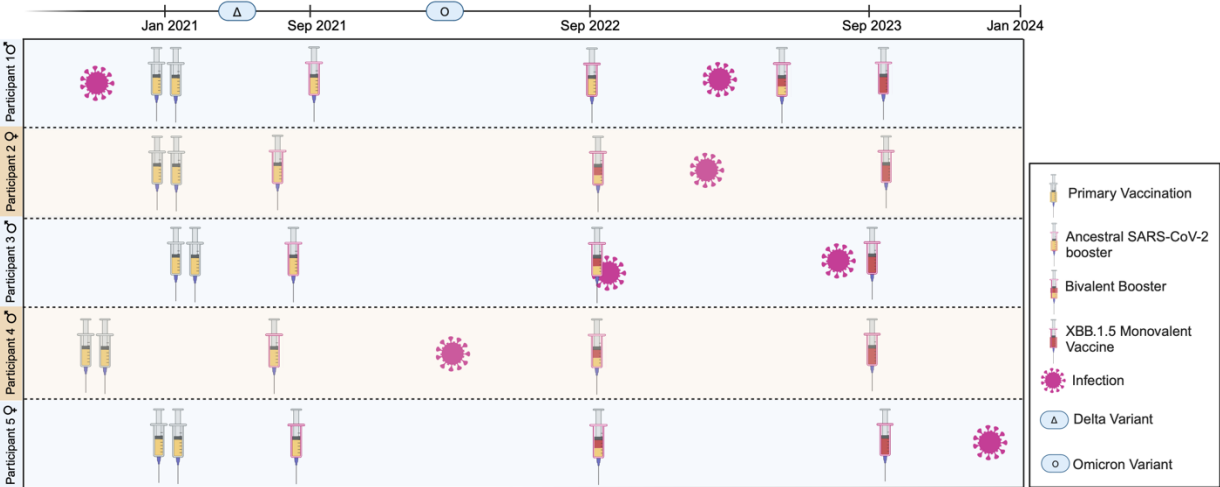
987
988   **Figure 1. SARS-CoV-2 Immune history of enrolled participants.** Participants 1, 2, and 3 received XBB.1.5
989   mRNA vaccination, while 4 and 5 received the recombinant protein XBB.1.5 vaccine. Delta and Omicron
990   variant's timeline reflects the United States of America. Created with BioRender.com.
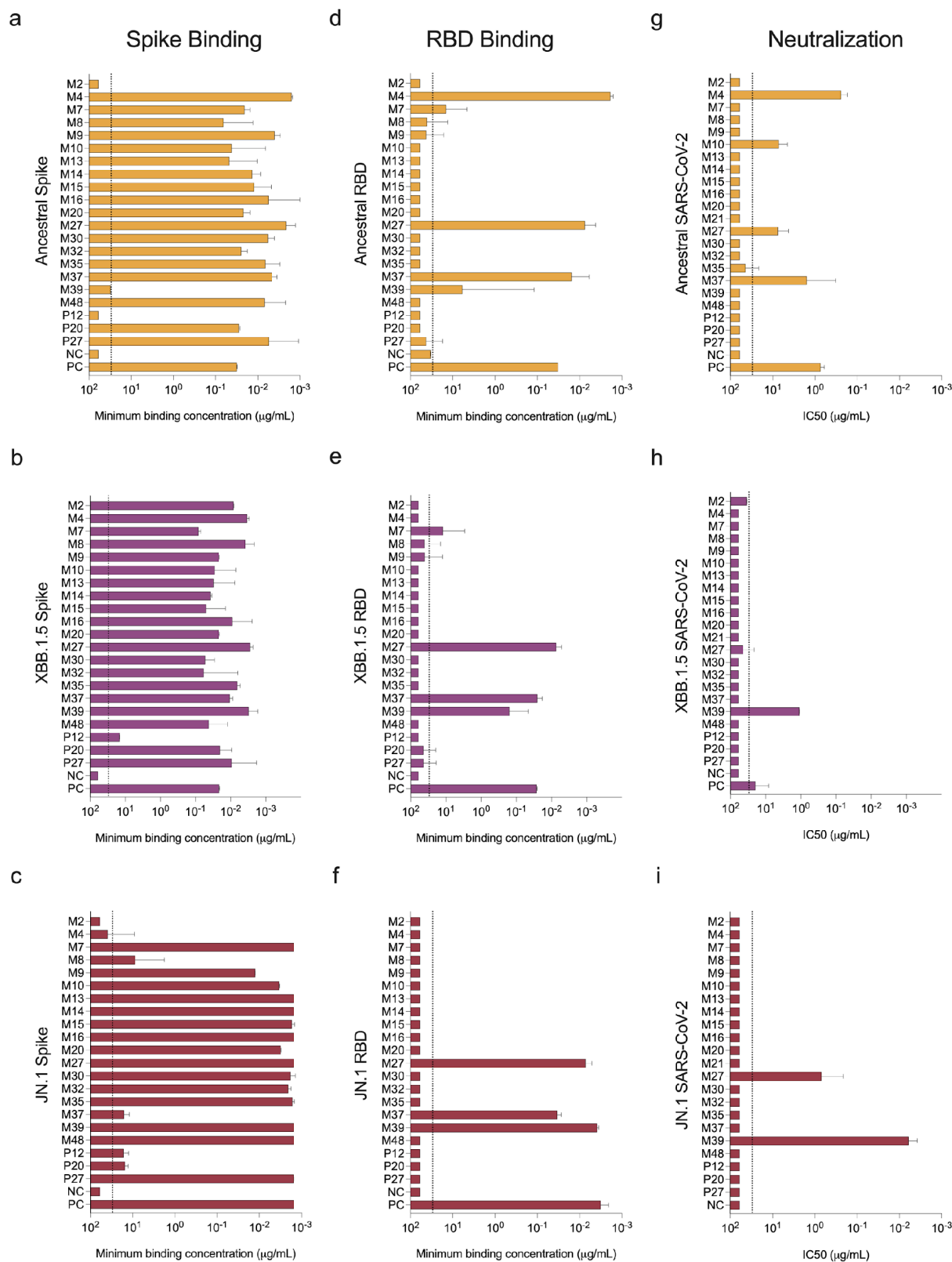
Figure 2. Binding and neutralizing capacity of monoclonal antibodies isolated from participants vaccinated with either mRNA or protein-based SARS-CoV-2 XBB.1.5 vaccines (a – c) Binding activity of

994   the 21 selected mAbs against ancestral, XBB.1.5 and JN.1 spike protein and **(d -f)** ancestral, XBB.1.5 and
995   JN.1 RBD. Neutralizing capacity of binding mAbs against **(g)** ancestral, **(h)** XBB.1.5, and **(k)** JN.1 SARS-
996   CoV-2. Antibodies from the mRNA group are represented by the letter M and protein-based by the letter
997   P. Antibodies that did not bind any antigen are not shown. Only mAbs binding to at least one antigen
998   were selected for the *in vitro* neutralization assays. The dashed line represents the limit of detection (LOD),
999   which is set at the starting dilution of 30 µg/mL. Binding is defined by minimum binding concentration
1000   (µg/mL) and neutralization is determined by half-maximal inhibitory concentration (IC$_{50}$). Negatives were
1001   assigned half the LOD.
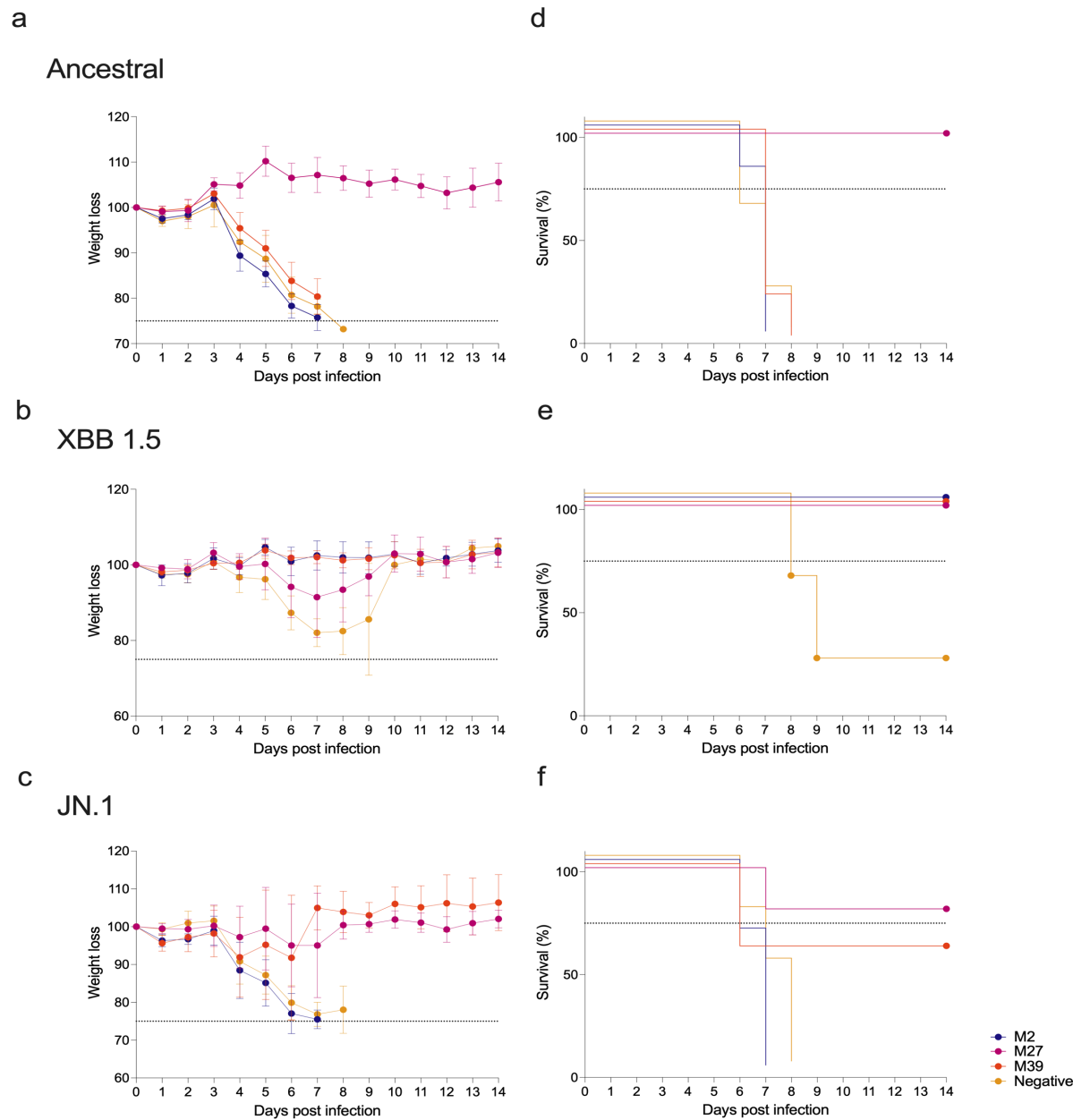1002
1003

1004
1005   **Figure 3:** *In vivo* **protection by prophylactic treatment with mAbs M2, M27 and M39. (a – c)** Weight
1006   loss in mice treated with 10 mg/kg (intraperitoneally) of M2, M27, or M39 mAbs two hours before

1007   challenge with a $3xLD_{50}$ dose of **(a)** WA1/2020, **(b)** XBB.1.5 and **(c)** JN.1. **(d – f)** Survival curves of mice
1008   treated with M2, M27, or M39 mAbs and infected with **(d)** WA1/2020, **(e)** XBB.1.5, and **(c)** JN.1. An
1009   influenza virus anti-hemagglutinin mAb, CR9114, was utilized as a negative control. Antibodies from the
1010   mRNA group are represented by the letter M and protein-based by the letter P.

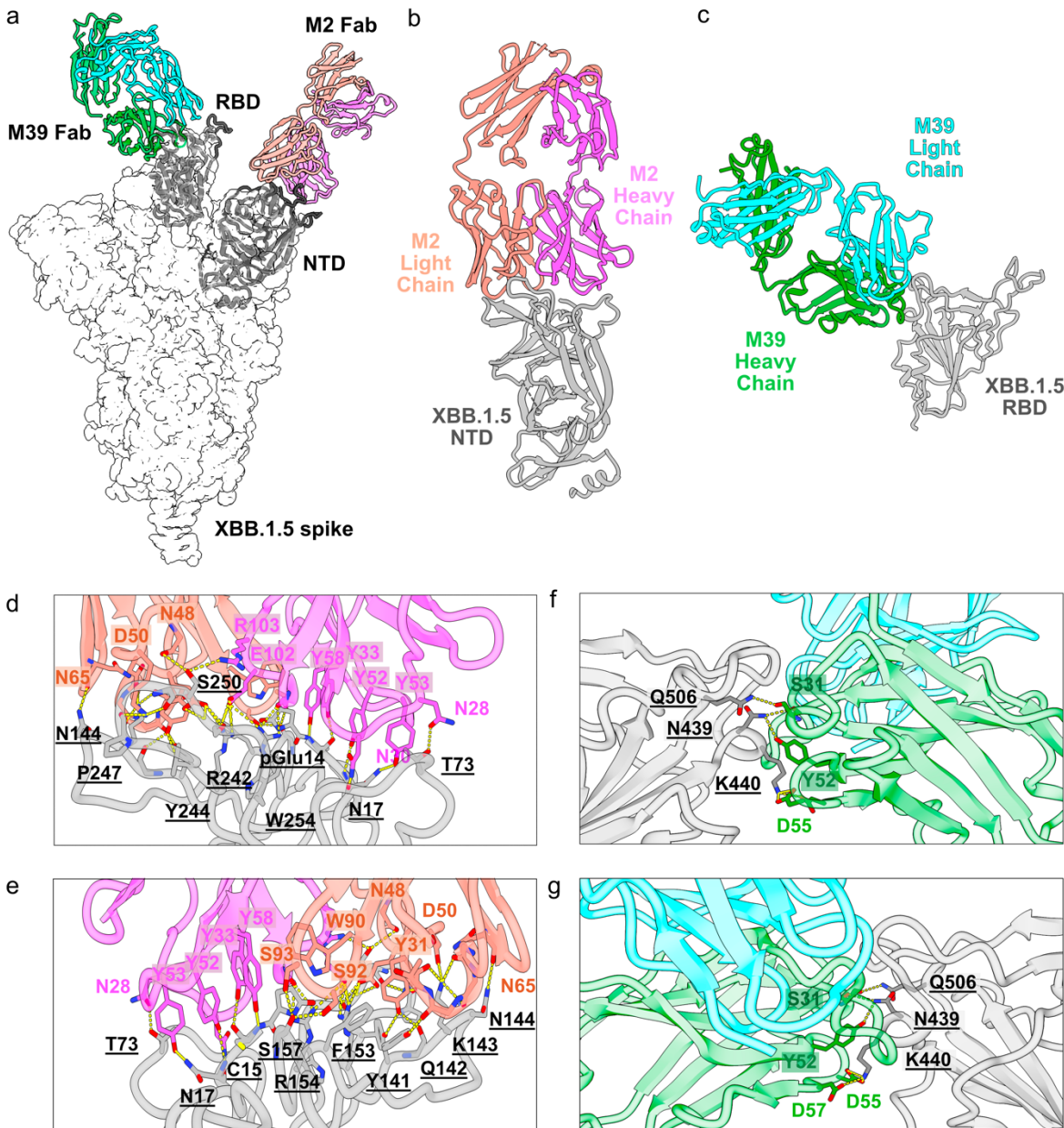1011

1012

1013

1014

1015
1016   **Figure 4. Cryo-EM structures of M2 and M39 Fabs in complex with XBB.1.5 spike. (a)** Surface regions
1017   of the SARS-CoV-2 spike contacted by the two antibodies M2 and M39. The global composite cryo-EM

1018   map is shown as a transparent surface, with the NTD:M2 Fab and RBD:M39 Fab complexes docked and
1019   shown in cartoon representation. **(b)** The M2 Fab defines an epitope on the "top" side of the NTD. M2
1020   creates an extensive surface contact area and engages NTD with both its heavy and light chains. **(d)** and
1021   **(e)** are two 180° views along the y-axis that show details of the intermolecular interactions between the
1022   M2 Fab and NTD with numerous polar and non-polar interactions. p-GLU designates pyroglutamate. **(c)**
1023   The M39 Fab defines an epitope on RBD engaged by numerous published "class 3" antibodies. M39 **(f)**
1024   and **(g)** are two 180° views along the y-axis that show details of the M39 Fab:RBD molecular interface with
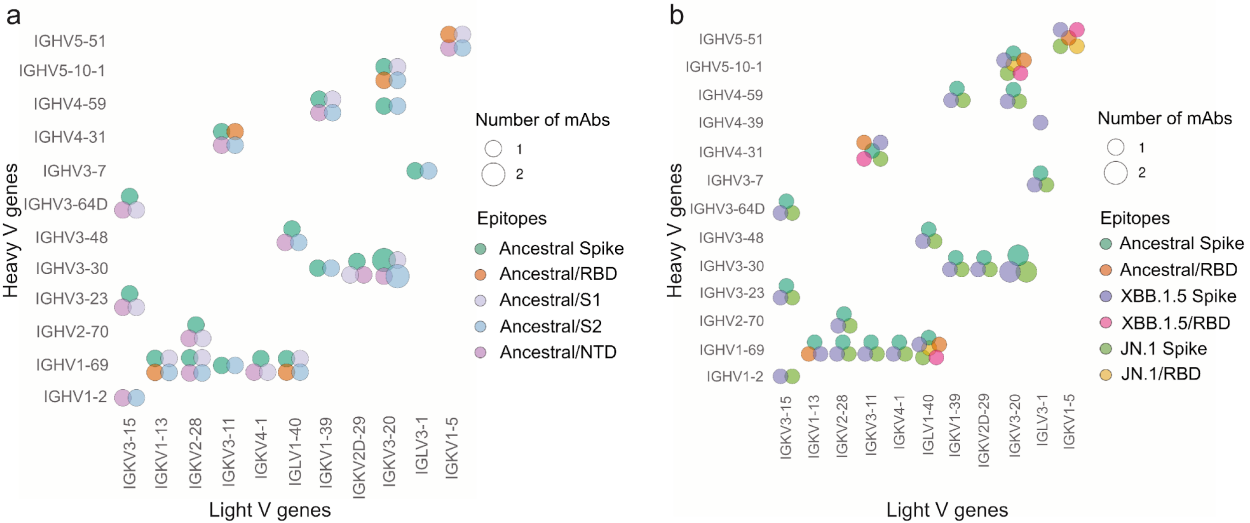1025   very few interacting residues forming salt bridges.
1026
1027

1028
1029   **Figure 5. Usage of antibody V gene in heavy and light chain of monoclonal antibodies targeting SARS-**
1030   **CoV-2 spike protein epitopes. (a)** V gene pairings for monoclonal antibodies targeting the entire
1031   ancestral spike protein, as well as the RBD, NTD, and S1 and S2 subunits. **(b)** V gene pairings for
1032   monoclonal antibodies targeting the entire ancestral spike protein, XBB.1.5, and JN.1 variants, along with
1033   their respective RBD domains. The size of each circle indicates the number of monoclonal antibodies that
1034   use the corresponding V gene pair and bind to the specified epitope. The definition of positive binding
1035   was determined based on the cutoffs from Figure 2 and Supplementary Figure S3.
1036

1037

1038

1039

1040

1041

1042

1043

SUPPLEMENTARY MATERIAL

PVI study group:

In alphabetical order: Harm van Bakel[1,2], Yuexing Chen[1,2], Christian Cognigni[1,2], Dylan Fitzgerald[1,2], Charles R. Gleason[1,2], Ana Gonzalez-Reiche[1,2], Morgan van Kesteren[1,2], Giulio Kleiner[1,2], Neko Lyttle[1,2], Jacob D. Mauldin[1,2], Jacob Mischka[1,2], Brian C. Monahan[1,2], Emilia Mia Sordillo[5], Reima Ramsamooj[1,2]

1. Department of Microbiology, Icahn School of Medicine at Mount Sinai, New York, NY, USA

2. Center for Vaccine Research and Pandemic Preparedness, Icahn School of Medicine at Mount Sinai, New York, NY, USA

3. Department of Pathology, Molecular and Cell-Based Medicine, Icahn School of Medicine at Mount Sinai, New York, NY, USA

4. The Global Health and Emerging Pathogens Institute, Icahn School of Medicine at Mount Sinai, New York, NY, USA

5. Division of Infectious Diseases, Department of Medicine, Icahn School of Medicine at Mount Sinai, New York, NY, USA

6. Precision Immunology Institute, Icahn School of Medicine at Mount Sinai, New York, NY, USA

Address: 1 Gustave Levy Place, Annenberg, 17th floor - New York, NY 10029

Phone number: 212-241-7393

E-mail: *virology@mssm.edu*

Figure S1. Antibody gene repertoire of mRNA- and Protein-based XBB.1.5 monovalent vaccine. (a) Frequency of nucleotide mutations in the V gene of heavy and light chain loci of plasmablasts from participants immunized with mRNA- or recombinant protein monovalent vaccines. **(b)** Antibody isotype frequency. IGHD and IGHE cells were removed from visualization. **(c)** V gene mutations in IgA and IgG sequences. **(d)** V gene mutations in IgG1. **(e)** HCDR3 length. **(f)** Relative volumes of aliphatic side chains (Ala, Val, Ile, and Leu) in the CDR3 region. **(g)** Frequency of aromatic amino acids (His, Phe, Trp, and Tyr) in the CDR3 region. Significant p-values are shown as follows: $p \leqslant 0.05$: *; $p \leqslant 0.01$: **; $p \leqslant 0.001$: ***; $p \leqslant 0.0001$: ****.
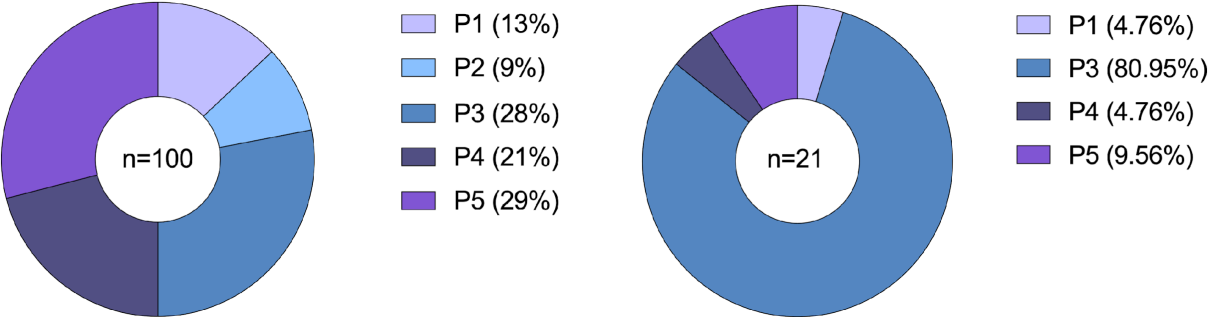
Figure S2. Distribution of 100 mAbs expressed across the five participants. (a) Total mAbs screened in the study. **(b)** mAbs showing binding positivity in ELISA.
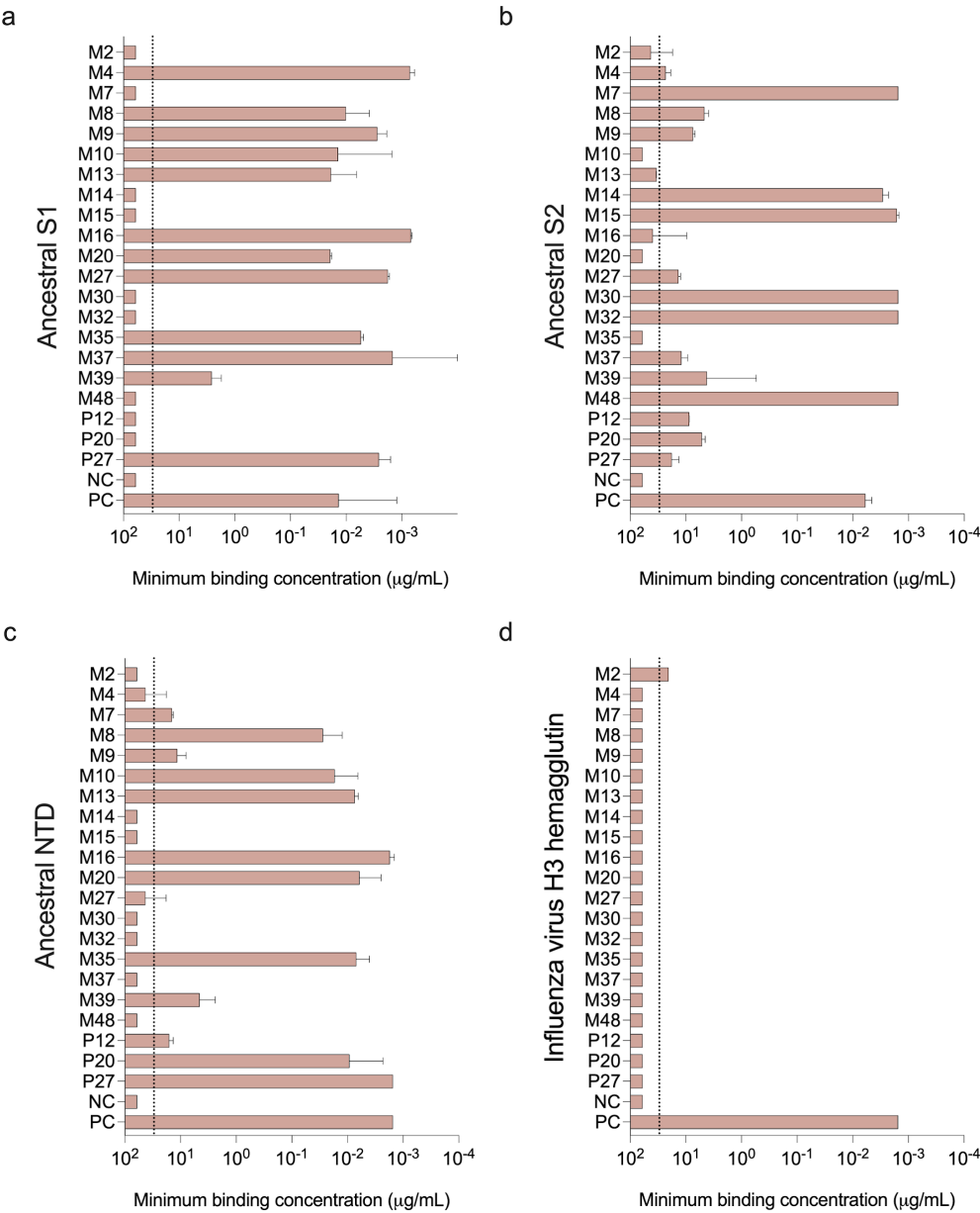
1097
1098

1099

Figure S3: Binding capacity of monoclonal antibodies isolated from participants vaccinated with either mRNA or protein-based SARS-CoV-2 XBB.1.5 vaccines against (a) Ancestral S1, **(b)** ancestral S2, **(c)** ancestral NTD, and **(d)** an irrelevant influenza virus H3 hemagglutinin (negative control). mAbs that did not bind to any antigen were excluded from the graphs. Dashed line represents the limit of detection (LOD) which is set at the starting dilution of 30 ug/mL. Binding is defined by minimum binding concentration (μg/mL). Negative antibodies were assigned half of the LOD for graphing purposes.
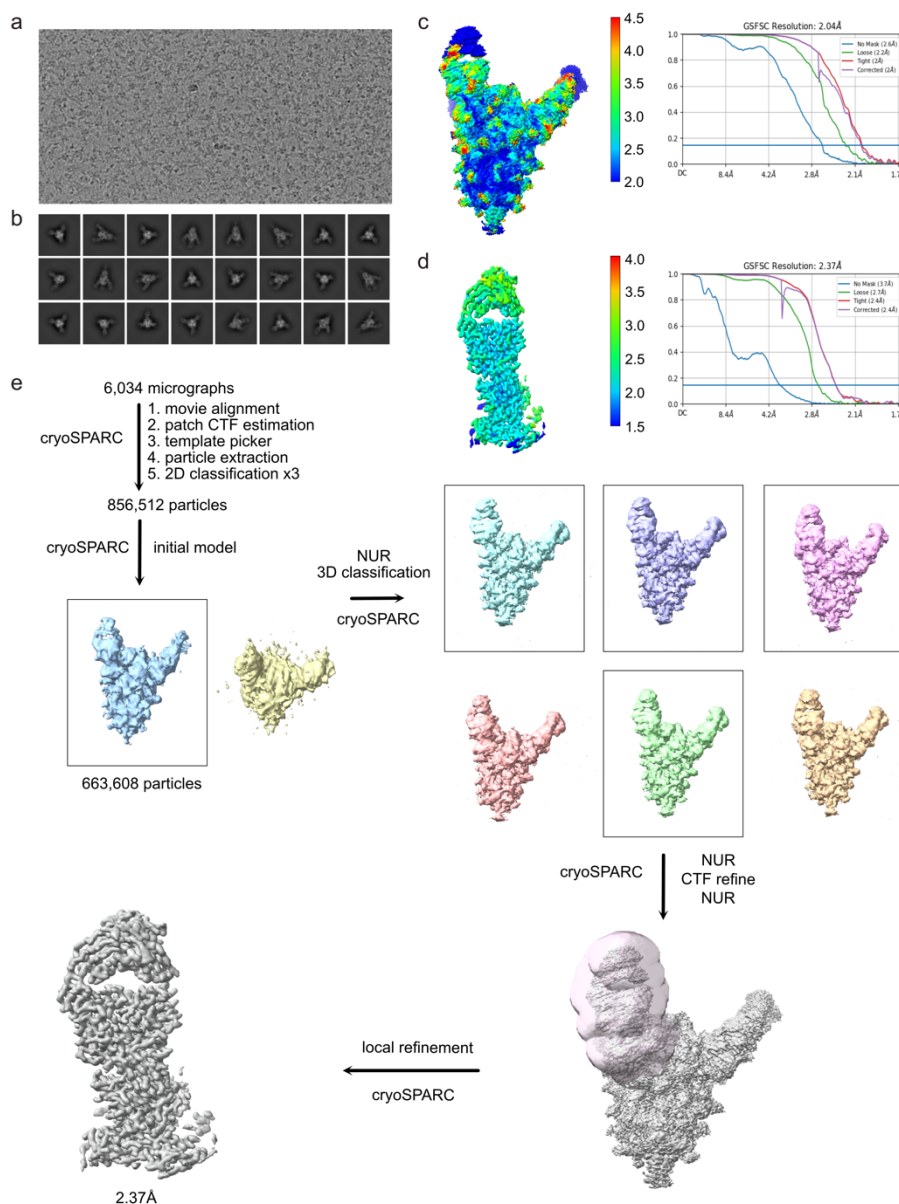
1106

1107

1108
1109

Figure S4: Cryo EM data processing and local resolution estimation. (a) Representative electron micrograph **(b)** 2D class average obtained for SARS-CoV-2 XBB.1.5 spike ectodomain in complex with Fab M2. Local resolution and gold-standard Fourier shell correlation curves calculated with cryoSPARC v4.3.1. **(c)** for overall **(d)** and locally refined, NTD-Fab complex. **(e)** Detailed cryo-EM data processing workflow.
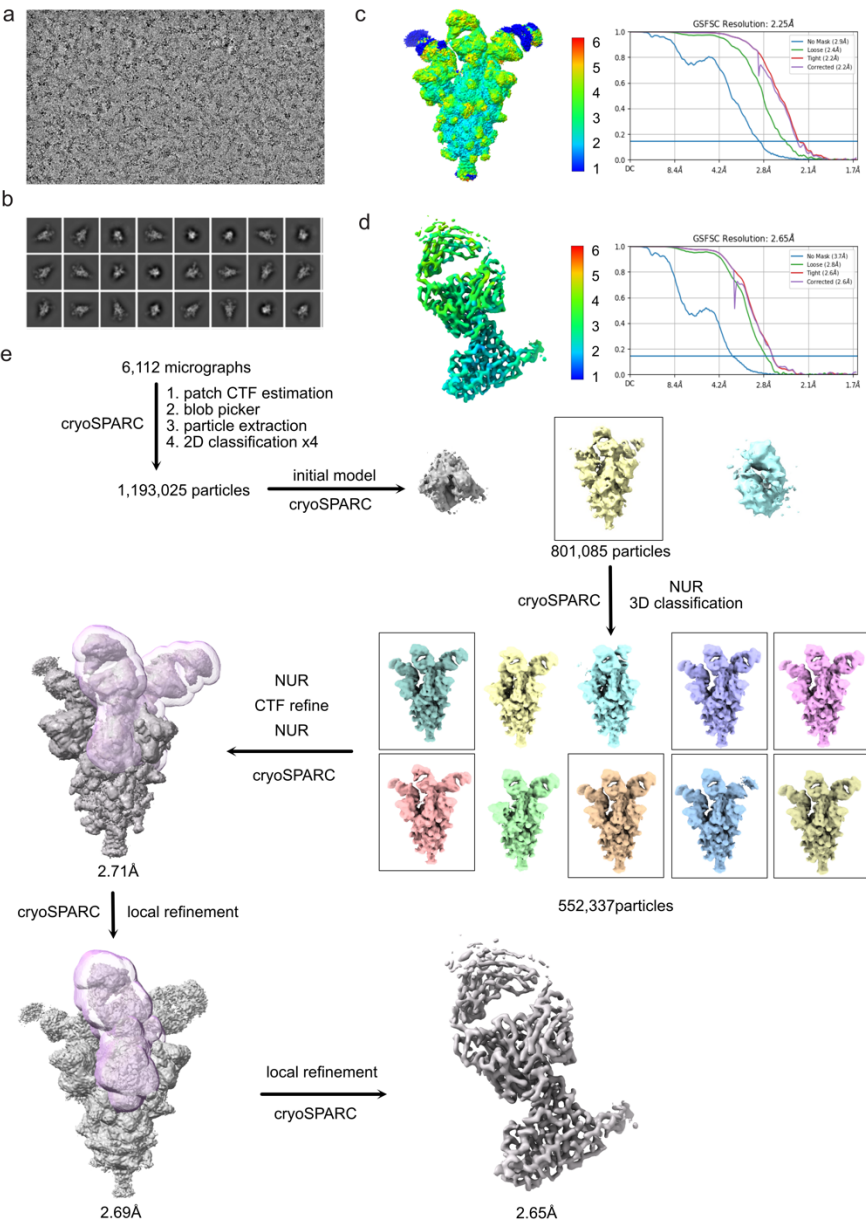
1114

1115

1116

Figure S5: Cryo EM data processing and local resolution estimation (a) Representative electron micrograph **(b)** 2D class average obtained for SARS-CoV-2 XBB.1.5 spike ectodomain in complex with M39 Fab. Local resolution and gold-standard Fourier shell correlation curves calculated with cryoSPARC v4.3.1. **(c)** for overall **(d)** and locally refined, RBD-Fab complex. **(e)** Detailed cryo-EM data processing workflow.
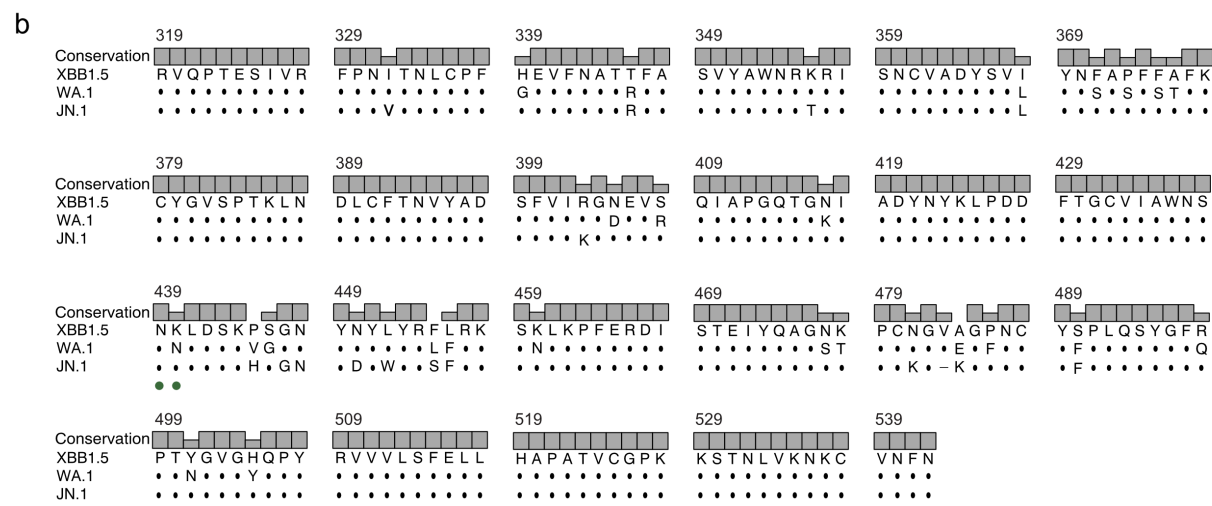
Figure S6: Multiple Sequence alignment **(a)** SARS-CoV-2 spike NTD (aa 14-302) of XBB.1.5, WA.1 and JN.1 **(b)** SARS-CoV-2 spike RBD (aa 319-542) of XBB.1.5, WA.1 and JN.1. Epitope residues of Fab M2 and M39 are indicated with colored dots.

Figure S7. Gating strategy for plasmablasts from participant P2, 6 days post XBB.1.5 booster.
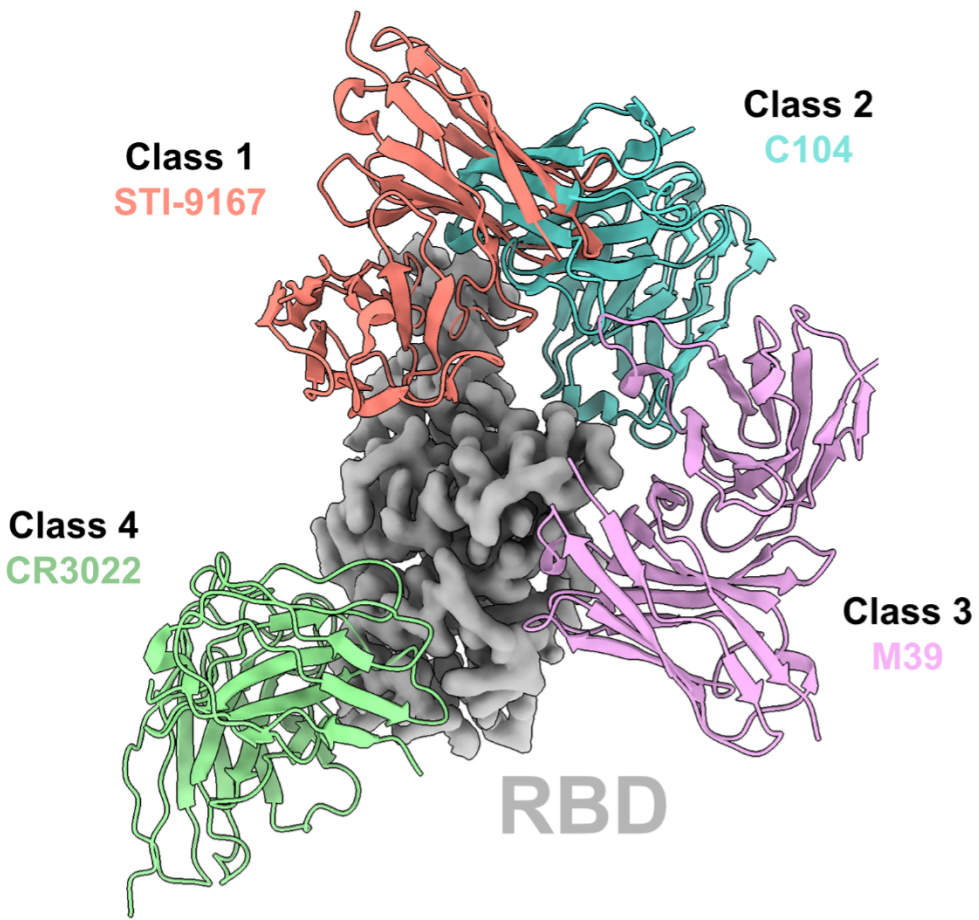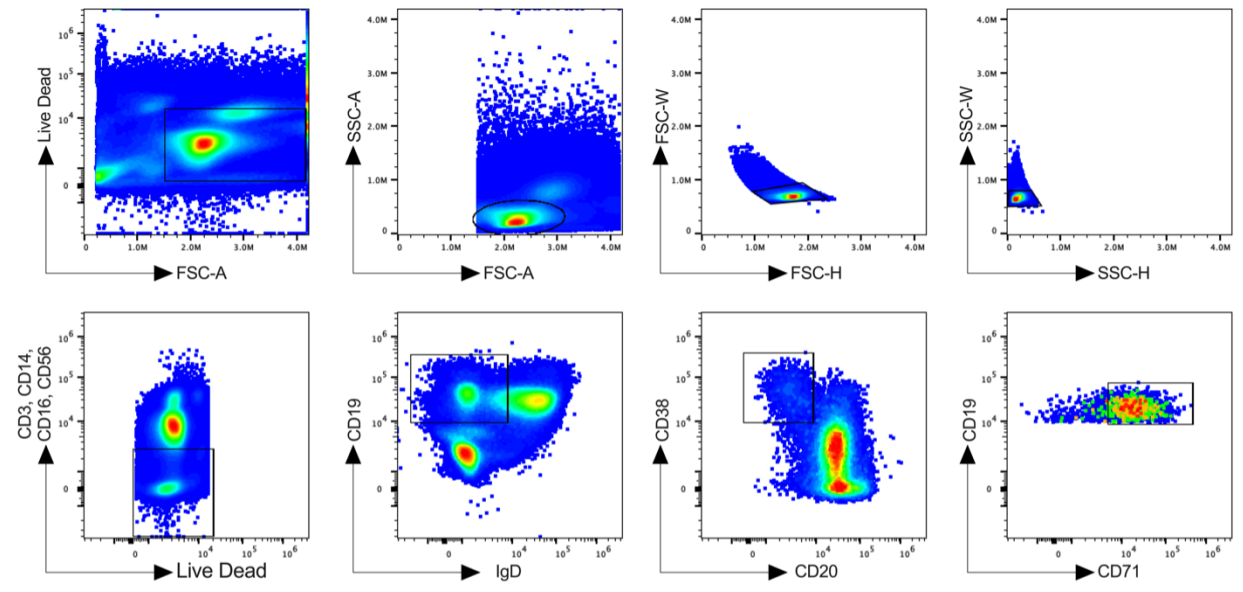
Figure S8: Structural illustration of representative Fabs from each class binding to its RBD epitope showing M39 as a class 3 antibody. Class 1 (STI-9167 *(62)*; PDB ID 8EQF), Class 2 (C104 *(45)*; PDB ID 7K8U), Class 3 (M39, PDB ID 9CCJ), Class 4 (CR3022 *(63)*; PDB ID 6YLA).

Appendix Tables

Participant ID	Platform	Timepoint	Number of heavy chain sequences before quality control	Number of light chain sequences before quality control	Number of heavy/light paired sequences after quality control
P1	mRNA	7	65	80	61
P2	mRNA	6	69	87	57
P3	mRNA	7	122	168	95
P4	Protein	7	205	220	201
P5	Protein	7	194	220	189

Table S1: Number of heavy and light chain pairs recovered from each participant.

Participant ID	Days post-vax	Cell type	Viability
P1	7	Plasmablasts	94%
P2	6	Plasmablasts	98%
P3	7	Plasmablasts	98%
P4	7	Plasmablasts	97%
P5	7	Plasmablasts	97%

Table S2: Viability (in %) of human PBMCs used in sorting experiments.

Antibody	Vendor	Catalog Number	Dilution
CD19 BUV563	BD Biosciences	612916	1:200
IgD Pacific Blue	Biolegend	348224	1:50
CD20 BV510	Biolegend	302340	1:100
CD3 PerCP	Biolegend	344814	1:100
CD14 PerCP	Biolegend	367152	1:200
CD16 PerCP	Biolegend	302030	1:200
CD56 PerCP	Biolegend	318342	1:200
CD38 AF810	Biolegend	334120	1:200
CD71 PE/Dazzle594	Biolegend	334120	1:200

Table S3: Antibodies Used for Flow Cytometry.

Data Collection		
	PDB ID 9CCJ and EMD-45444	PDB ID 9CCI and EMD- 45443
Grid type	UltrAuFoil gold R1.2/1.3	UltrAuFoil gold R1.2/1.3
Microscope/voltage/detector	Titan Krios/300 kV/Gatan K3 summit	Titan Krios/300 kV/Gatan K3 summit
Magnification	105,000	105,000
Recording mode	counting	counting
Total dose	49.883 e-/Å^2/s	49.883 e-/Å^2/s
Pixel size	0.825 Å/pixel	0.825 Å/pixel
Defocus range	0.6 to 2.4 μm	0.6 to 2.5 μm
No. micrographs used	6,034	6,112
Total particles picked	856,516	1,193,025
Model Validation		
Composition (#)		
Chains	3	3
Atoms	5410	4921
Residues	Protein: 686 Nucleotide: 0	Protein: 631 Nucleotide: 0
Ligands	NAG: 7, BMA:1	NAG: 1
Bonds (RMSD)		
Length (Å) (# > 4sigma)	0.008 (2)	0.005 (0)
Angles (°) (# > 4sigma)	1.346 (11)	0.871 (2)
MolProbity score	1.40	1.21
Clash score	2.35	1.66
Ramachandran plot (%)		
Outliers	0.30	0.00
Allowed	5.38	4.19
Favored	94.32	95.81
Rotamer outliers (%)	0.00	0.00
Cbeta outliers (%)	NA	NA
Peptide plane (%)		
Cis proline/general	7.3/0.0	5.3/0.0
Twisted proline/general	0.0/0.0	0.0/0.0
CaBLAM outliers (%)	2.75	2.29
Data		
Lengths (Å)	74.25, 93.22, 127.05	72.60, 97.35, 142.72
Angles (°)	90.00, 90.00, 90.00	90.00, 90.00, 90.00
Supplied Resolution (Å)	2.4	2.6
Resolution Estimates (Å)	Masked	Masked
d FSC (half maps; 0.143)	2.4	2.6
d 99 (full/half1/half2)	2.0/1.7/1.7	2.2/1.9/1.9
d model	1.6	1.7

D FSC model (0/0.143/0.5)	1.4/1.5/2.2	1.4/1.6/3.0
Map min/max/mean	-0.00/1.83/0.01	-0.00/1.66/0.02
Model vs. Data		
CC (mask)	0.84	0.81
CC (box)	0.81	0.58
CC (peaks)	0.78	0.39
CC (volume)	0.84	0.81
Mean CC for ligands	0.67	0.69

1151   Table S4: Cryo-EM data collection and model validation statistics.

1152

1153

1154

1155

1156

1157

1158